Crystallographic superstructure in R_2PdSi_3 compounds (R = heavy rare earth)

Fei Tang (唐菲),[1,*] Matthias Frontzek,[1,2] Julia Dshemuchadse,[3,4] Tilmann Leisegang,[4,5] Matthias Zschornak,[4,5,6] Robert Mietrach,[4] Jens-Uwe Hoffmann,[7] Wolfgang Löser,[8] Sibylle Gemming,[5] Dirk C. Meyer,[9] and Michael Loewenhaupt[1]

[1]*Institut für Festkörperphysik, TU Dresden (TUD), D-01062 Dresden, Germany*

[2]*Neutron Scattering Science Division, Oak Ridge National Laboratory, Oak Ridge, Tennessee 37830 United States*

[3]*Laboratory of Crystallography, ETH Zurich, CH-8093 Zurich, Switzerland*

[4]*Institut für Strukturphysik, TUD, D-01062 Dresden, Germany*

[5]*Helmholtz-Zentrum Dresden Rossendorf, P. O. Box 510119, D-01314 Dresden, Germany*

[6]*Institut für Experimentalphysik, TU BA Freiberg, D-09599 Freiberg, Germany*

[7]*Helmholtz-Zentrum-Berlin (HZB), Hahn-Meitner-Platz 1, D-14109 Berlin, Germany*

[8]*Leibniz-Institut für Festkörper- und Werkstoffforschung (IFW) Dresden, D-01069 Dresden, Germany*

[9]*Institut für Experimentelle Physik, TU Bergakademie Freiberg, D-09599 Freiberg, Germany*

(Received 10 February 2011; revised manuscript received 27 June 2011; published 7 September 2011)

The R_2PdSi_3 intermetallic compounds have been reported to crystallize in a hexagonal AlB_2-derived structure, with the rare earth atoms on the Al sites and Pd and Si atoms randomly distributed on the B sites. However, the intricate magnetic properties observed in the series of compounds have always suggested complications to the assumed structure. To clarify the situation, x-ray and neutron diffraction measurements were performed on the heavy rare earth compounds with R = Gd, Tb, Dy, Ho, Er, Tm, which revealed the existence of a crystallographic superstructure. The superstructure features a doubled unit cell in the hexagonal basal plane and an octuplication along the perpendicular $\boldsymbol{c}$ direction with respect to the primitive cell. No structural transition was observed between 300 and 1.5 K. Extended x-ray absorption fine structure (EXAFS) analysis as well as density functional theory (DFT) calculations were utilized to investigate the local environments of the respective atoms. In this paper the various experimental results will be presented and it will be shown that the superstructure is mainly due to the Pd-Si order on the B sites. A structure model will be proposed to fully describe the superstructure of Pd-Si order in R_2PdSi_3. The connection between the crystallographic superstructure and the magnetic properties will be discussed in the framework of the presented model.

DOI: 10.1103/PhysRevB.84.104105 PACS number(s): 61.66.Dk, 75.25.−j

I. INTRODUCTION

The various rare earth intermetallic compounds have been the focus of scientific research for 50 years. A variety of new and highly specific physical properties, such as superconductivity, heavy fermions, Fermi-liquid behavior, quantum-phase transitions, etc., have been unveiled which delicately depend on the smallest variations of the chemical composition. In this respect, the ternary rare earth compounds R-T-X (R = rare earth, T = transition metal, and X = main-group element) are of great relevance since the interplay between magnetic (rare earth) and nonmagnetic (X) atoms, and the influence of a transition metal on the electronic properties can be studied. The R_2TSi_3 compounds (R = rare earth or uranium) are of particular interest since they crystallize in a highly symmetric AlB_2-type crystal structure. Although they have been investigated for about 30 years, the published results on the crystal structure have been conflicting. This is probably due to the lack of single-crystalline samples in the earlier studies and the variations in the sample growing processes, the latter of which, as will be shown, also plays a role in the crystal structure.

The hexagonal AlB_2-structure (space group $P6/mmm$) represents one of the simplest inorganic crystallographic structures. The Al atoms are on position $\boldsymbol{r}_0 = (0, 0, 0)$ while the B atoms occupy positions $\boldsymbol{r}_1 = (\frac{1}{3}, \frac{2}{3}, \frac{1}{2})$ and $\boldsymbol{r}_2 = (\frac{2}{3}, \frac{1}{3}, \frac{1}{2})$ in the primitive unit cell (Wyckoff sites $1a$ and $2d$[1]). Throughout the paper this structure will be referred to as "main" structure and its unit cell as the "primitive" cell. These lattice constants for the investigated compounds are listed in Table I.

The AlB_2 structure is a layered structure where Al layers are separated by B layers. A sketch of the structure is shown in Fig. 1.

So far, 46 structure types of binary and ternary intermetallic compounds are known to be derived from the AlB_2 structure.[2] For example, the binary compounds RSi_2 (R = heavy rare earth or uranium as in β-USi_2[3]), from which the ternary R_2TSi_3 compounds are derived, crystallize also in AlB_2-type structure, with the R atoms occupying the $1a$ sites and Si on the $2d$ sites exclusively.[4,5] Silicon deficiency has been observed in most RSi_2 compounds with R = heavy rare earth leading to vacancies on the $2d$ sites (for instance in $YbSi_{2-x}$[6]).

In the ternary R_2TSi_3 compounds,[7,8] an important question arises: With the Si deficiency compensated by the additional transition metal atoms, how does the crystal structure adapt itself? That is, do the transition metal atoms and Si atoms mix freely or do they order in a specific manner? The transition metals with which compounds have been synthesized are, without claiming completeness: Ru (1.3),[9] Os (1.3), Ir (1.35),[10] Co (1.35),[11] Rh (1.35),[12] Pt (1.35),[13,14] Cu (1.35),[15] Fe (1.4),[16] and Pd (1.4).[17] In parentheses are the atomic radii in solids in Ångstroms according to Slater.[18] Although the Si-Si distance in these compounds is close or actually smaller than the bond length found in elemental silicon (2.35 Å),[12] it is assumed that the introduction of quite differently sized transition metal ions leads to the same crystallographic structure.

TABLE I. Lattice parameters for R_2PdSi_3 from single crystal diffraction at $T = 2$ and 300 K. The lattice constants were determined from one main Bragg peak and are therefore not as precise as values obtained from a full refinement. Please see Szytula *et al.*[20,41] for values from refined powder diffractograms.

	T = 300 K		T = 2 K	
R	a (Å)	c (Å)	a (Å)	c (Å)
Gd	4.079	4.098	4.066	4.091
Tb	4.048	4.037	4.043	4.024
Dy	–	–	4.06	4.03
Ho	4.076	4.021	4.073	3.959
Er	4.064	3.991	4.059	3.986
Tm	4.057	3.970	4.051	3.966

In the series U_2RuSi_3, U_2RhSi_3, and U_2PdSi_3 a superstructure has been observed which leads to a doubling of the a parameter. The superstructure, which is due to T-Si ordering, degrades from a completely site-ordered variant for U_2RuSi_3 to a variant of randomly occupied $2d$ sites for U_2PdSi_3, although for the latter, weak diffuse scattering from a superstructure was still observed.[8] The systematics have been explained by the increasing electron number in the d shells. It has been assumed that the larger electron number is counteracting the formation of Si-Hueckel arenes.

In comparison, less compounds with rare earth elements have been synthesized so far, notably only R_2RhSi_3,[12] R_2PtSi_3,[14] and R_2PdSi_3[19] could be obtained for a larger number of rare earth atoms. The R_2RhSi_3 compounds are so far the most investigated compounds. They exhibit a superstructure which doubles both lattice parameters a and c.[12] The ordering on the $2d$ sites seems to be due to the formation of Si-Hueckel arenes.[2] In this structure the Rh atoms have only Si atoms as nearest neighbors. The R_2PtSi_3 compounds are assumed to have a similar superstructure although experimental evidence is ambiguous.[14]

The family R_2PdSi_3 (R = heavy rare earth) has attracted much attention since it was first investigated by Kotsanidis *et al.*[19] due to the complex and novel magnetic properties found in the series.[20–26] All investigated compounds with R = Gd, Tb, Dy, Ho, Er, Tm order antiferromagnetically with Néel temperatures between 2 and 23 K. The ordering temperature for Tm_2PdSi_3 ($T_N = 1.8$ K[27]) was reported later. The ordering temperatures do not seem to follow the DeGennes rule[28] as the heavy rare earth metals. Moreover, the magnetic susceptibility as a function of temperature shows nontrivial behavior and implies complicated magnetic structures with the coexistence of anti- and ferromagnetic interactions. The crystal structure has been initially reported to be similar to the R_2RhSi_3 compounds (doubled unit cell in both inequivalent directions).[19] First neutron diffraction experiments on powder samples by Szytula *et al.*[20] indicated, however, a primitive AlB_2-type structure with randomly occupied $2d$ sites, which is the up to now accepted crystal structure. The lattice constants (Table I) are around 4 Å for both a and c throughout the series.

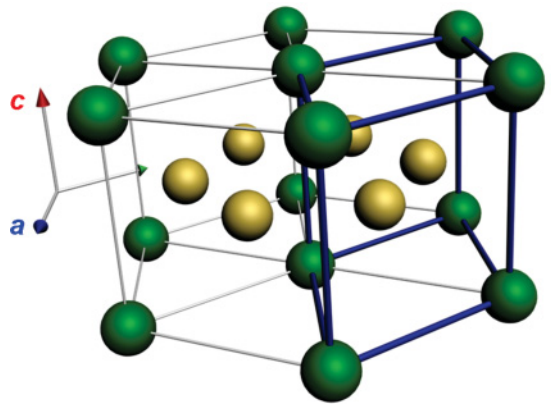

FIG. 1. (Color online) The basic AlB_2 structure. In green are atoms on the $1a$ sites (0, 0, 0), in gold are the atoms occupying the $2d$ sites ($\frac{1}{3}$, $\frac{2}{3}$, $\frac{1}{2}$) and ($\frac{2}{3}$, $\frac{1}{3}$, $\frac{1}{2}$). The c to a ratio is close to one.

On the other hand, there were already hints for the existence of a crystallographic superstructure in the R_2PdSi_3 series from the very early studies. X-ray investigations by Kotsanidis *et al.*[19] suggested the unit cell parameter a to be around 8 Å, twice the currently recognized values. A superstructure with a ($2a$, $2a$, $4c$) unit cell for Ce_2PdSi_3 has also been reported.[29] Later neutron diffraction experiments on powder samples[20] showed the occurrence of nonindexable reflections when the primitive cell notation (a, a, c) was assumed.

Not only the structure investigation, but also the observed complex magnetic properties, give rise to speculations concerning a superstructure. With the availability of large high-quality single crystals[30–32] more detailed studies have been performed on the series of compounds to clarify the magnetic properties as well as the crystal structure.[27,33–36] In R_2PdSi_3 single crystals, weak additional reflections were observed by x-ray diffraction[37] and neutron scattering[27] with no structural phase transition between room and very low temperatures (down to 1.5 K). Furthermore, a systematic study on the single crystals with ac susceptibility, magnetization measurements, and neutron scattering revealed a generic phase in the field-temperature phase diagram in this series.[27,38] The magnetic structure of the generic phase yields additional intensity on the extra reflections. The generic phase is therefore closely related to the crystallographic superstructure in these compounds. To understand the properties of the generic phase and other magnetic properties in the series brings the need to clarify the crystal structure of the R_2PdSi_3 compounds.

Here we report on a comprehensive investigation of the crystal structure of high-quality single crystals of composition R_2PdSi_3 where R are heavy rare earths. This survey on the crystallographic superstructure is based on a wide spectrum of collected experimental data, including x-ray diffraction (XRD), neutron diffraction, and extended x-ray absorption spectroscopy (EXAFS). Experimental details for the various methods used can be found in Sec. II. In Sec. III details of the observed superstructure are presented. Results of extensive XRD on single crystalline Ho_2PdSi_3 and neutron diffraction on more single crystalline compounds with R = Gd, Tb, Dy, Ho, Er, Tm) are summarized therein. In Sec. IV total energy considerations concerning the local structure of Pd atoms are examined with DFT calculations and are compared with the local structure characterization by means of EXAFS experiments in Sec. V. A structural model based on the experimental observations is proposed using a modulation

approach with symmetry considerations (Sec. VI). In Sec. VII the significance of the superstructure and its implications for possible magnetic structures in the series are discussed. A summary can be found in Sec. VIII.

II. EXPERIMENTAL DETAILS

A. The samples

Single crystals were grown by floating zone methods with either radio frequency inductive heating or optical heating under purified Ar atmosphere at melting temperature >1500 °C from polycrystalline rods of 6 mm diameter and typically 55 mm in length.[30,32] The growth velocities were between 3 and 10 mm/h. Post solidification cooling rates of order of 10^2 K/h estimated from the measured temperature gradients on the crystal surface[39] may be compared with about 10^2 K/s for arc-melted samples. More experimental details are given elsewhere.[40,41] The resulting crystals were characterized by optical polarization microscopy and scanning electron microscopy. In some of the single crystals striation-like *R*Si or RSi_2 were detected which could be removed by annealing at temperatures up to 1200 °C for over 20 h and subsequent quenching. The chemical composition of crystals was characterized by electron probe microanalysis and for selected cases authenticated using inductively coupled plasma optical emission spectrometry (ICPOES). The resulting formula for the Ho compound is $Ho_2Pd_{1.01(1)}Si_{2.99(1)}$, in agreement with the nominal ratio 2 : 1: 3.

B. X-ray diffraction

Samples with a characteristic dimension of 50–200 μm were cut from the single crystalline Ho_2PdSi_3 rods and prepared for XRD analysis. Some samples were ground to a sphere in a dedicated apparatus[41] to minimize the influence of absorption on the reflection intensities. The diffraction patterns were recorded under ambient conditions ($T = 297$ K) using, first, a single crystal diffraction system equipped with an image plate detector (Stoe & Cie IPDS-1), and second, a four-circle diffractometer (Stoe & Cie STADI4) equipped with a scintillation detector. Both devices are equipped with a graphite monochromator and an x-ray tube generating characteristic Mo $K\alpha$ radiation ($\lambda_{\mathrm{Mo}\,K\alpha} = 0.71069$ Å). The first data set [$(\sin\theta/\lambda)_{\max} = 0.64$ Å^{-1}] was used for the detailed inspection of the diffraction pattern, the second one [$(\sin\theta/\lambda)_{\max} = 1.08$ Å^{-1}] was utilized for the structure refinements (details see Table II). All investigated crystals exhibit the same diffraction patterns. The data of two crystals, one spherical crystal (crystal 1, diameter is 150 μm) and a prismatic shaped crystal (crystal 2, dimension of $70 \times 70 \times 40$ μm^3) are presented here. $\lambda/2$ contributions of the primary radiation have been carefully inspected[42] and verified not to be the cause for the observed additional reflections (see Sec. III). Data reduction and processing were carried out with the diffractometers' software (STOE & Cie, 1999). For the application of the absorption correction and subsequent structure refinements, we applied the program JANA 2006.[43] Further details on the experiments are described by Dshemuchadse[37] and Leisegang.[41]

C. Neutron diffraction

Most of the neutron diffraction experiments on R_2PdSi_3 were carried out at the Helmholtz-Zentrum für Materialien und Energie GmbH (formerly Hahn-Meitner Institut) with the flat-cone diffractometer E2 before its upgrade (Gd_2PdSi_3 was measured on D9 at ILL, Grenoble). A graphite monochromator with additional pyrolytic graphite filters to suppress $\lambda/2$ contamination in the incident beam was employed to provide neutrons with wavelength $\lambda = 2.39$ Å. A standard-orange-type cryostat capable of reaching 1.5 K base temperature was used. Measurements were carried out both at room temperature and down to 1.5 K through the respective Néel temperature of the compound. The old E2 diffractometer employs a "banana"-type multidetector with 400 channels covering a scattering angle of $2\theta = 80°$. The sample was rotated around the axis perpendicular to the scattering plane in steps of $\Delta\omega = 0.2°$. Finally a ω-2θ map is obtained which can be transformed into a full reciprocal plane, easily allowing the search for yet unknown propagation vectors.

The samples for neutron diffraction were cut from the single crystalline rods and are mostly irregular in shape. Faces with certain directions are cut and polished after pre-orientation with a back-scattering Laue camera. The sample masses range from 0.4 to 2.7 g.

D. X-ray absorption spectroscopy

EXAFS[44] measurements were performed at beamline C (CEMO)[45] of the Hamburger Synchrotronstrahlungslabor (HASYLAB) at Deutsches Elektronen-Synchrotron (DESY). The room temperature measurements were conducted in transmission mode at a vacuum pressure of $p < 10^{-5}$ mbar. For selection of the primary beam photon energy a Si(111) (for the Pd K edge) or Si(311) (for the rare earth L edge) double crystal monochromator[46] was employed. The energy was calibrated using pure metallic foils. Primary and transmitted intensities were recorded with two independent gas ionization chambers using dedicated gas mixture (calculated with the program XAFSMASS[47]). The EXAFS spectra were collected at the Pd K and the R L absorption edges using the optimized scan parameters supplied by the beamline software. The energy ranges of the exciting photons are 6289–10800 eV for the R L edge and 24055–25305 eV for the Pd K edge. The energy step widths are $\Delta E \leqslant 10$ eV, $\Delta E = 0.5$ eV, and $\Delta E = 0.5$–2.5 eV, below, in the vicinity, and above the absorption edge, respectively. The varying energy step width above the absorption edge was chosen to ensure an equidistant step width in k space of $\Delta k = 0.05$ Å^{-1} for the EXAFS region of the spectra.

For $R =$ Ho and Er the powder samples were prepared from single crystal rods, while all other powder samples were prepared from the polycrystalline starting material. Powder samples with a specific amount—a product $\mu \cdot d$ of 1.5 (μ is absorption coefficient and d sample thickness) for every absorption edge was realized—were mixed with cellulose powder in a desired ratio and pressed to pills. A data reduction of the x-ray absorption spectra was first performed using the ATHENA software[48]. In this respect, the spectra were normalized to an edge jump of 1 and the absorption coefficient of the isolated atoms $\mu_0(E)$ was extracted by fitting a cubic

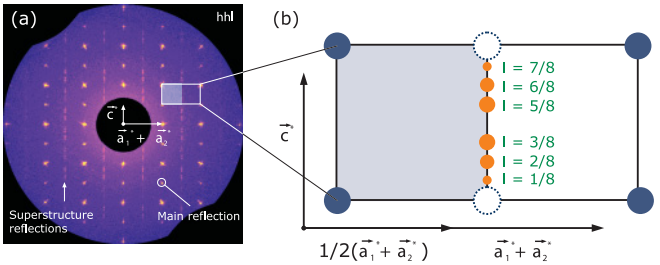

FIG. 2. (Color online) The *hhl* reciprocal plane of Ho_2PdSi_3: (a) experimental data at room temperature and (b) schematic representation. In the sketch the observed reflections are shown as filled circles, while open circles mark positions of not-observed reflections emanating from the doubling of unit cell parameter a.

spline function to the data. After subtraction of the atomic background, the conversion from E to k scale was performed. A quantitative analysis, that is, refinement of the EXAFS data, was subsequently done using the program ARTEMIS[48] based on the FEFF 6 code.[49] Structure parameters for the starting models (atom clusters) were taken from the single crystal x-ray diffraction analysis.

III. SINGLE CRYSTAL DIFFRACTION

Indexing of the diffraction patterns in the following is based on the primitive unit cell (a, a, c) notation. The reflections which can be indexed by integers will be referred to as main reflections.

A. X-ray diffraction on Ho_2PdSi_3

The x-ray diffraction pattern of the reciprocal $h0l$ plane of the Ho_2PdSi_3 single crystal is shown in Fig. 2 (comparable data have been also obtained for Gd_2PdSi_3). The strong main reflections can be indexed by a hexagonal unit cell with approximately $a = 4.05$ Å and $c = 4.00$ Å, corresponding to the primitive structure.

Apart from the main reflections, additional weak reflections (thereafter referred to as "superstructure reflections") are clearly visible at positions where h and/or k are half integers [orange circles in Fig. 2(b)]. This indicates a doubling of the unit cell in the basal plane. The corresponding l indices have values of $\frac{1}{8}$, $\frac{2}{8}$, $\frac{3}{8}$, etc., indicating an octuplication of the unit cell along the $\boldsymbol{c}$ direction. No intensities are observed at $l = 0$, $\frac{4}{8}$.

The superstructure reflections in the hk-reciprocal plane at $l = \frac{1}{8}$, $\frac{2}{8}$, and $\frac{3}{8}$ (figures not shown) exhibit a hexagonal, identical arrangement with the strongest intensities on the $hk\frac{3}{8}$ plane. Both main and superstructure reflections exhibit Laue symmetry $6/mmm$. Statistics about the collected reflections are tabulated in Table II. Averaging of reflections has been performed according to $P6/mmm$ symmetry.

B. Neutron diffraction on R_2PdSi_3 (R = Gd, Tb, Dy, Ho, Er, Tm)

Neutron diffraction experiments have been performed on more compounds with R = Gd, Tb, Dy, Ho, Er, Tm. Figure 3 shows the reciprocal *hhl* plane of a Tm_2PdSi_3 single crystal

TABLE II. Details of the x-ray diffraction measurements with the four-circle diffractometer Stoe & Cie STADI4 and data statistics.

Wavelength	$\lambda_{\mathrm{Mo}\,K\alpha} = 0.71069$ Å
Temperature	$T = 297$ K
2θ range	3.8°–100.1°
$\sin\theta_{\max}/\lambda$	1.08 Å^{-1}
Resolution $d_{\min}$	0.46 Å^{-1}
Absorption correction	numerical
hkl range	$-4 < h < 4$
	$-8 < k < 8$
	$-8 < l < 8$
Criterion for observed reflections	$I > 2\sigma(I)$
Number of reflections (observed/all)	3960/34 159
Averaged reflections (observed/all)	562/3746
Averaged main reflections (observed/all)	156/369
Averaged superstructure reflections (observed/all)	406/2897

as an example. An excellent qualitative and quantitative agreement between x-ray (Fig. 2) and neutron data (Fig. 3) can be seen.

Main reflections 110 and 002 as labeled in the figure, as well as 111 and 001 have been observed as expected from the primitive structure. The relative intensities of these reflections are in agreement with calculations from the primitive structure. Moreover, as shown in Fig. 3(b), superstructure reflections at the same positions as observed by XRD have been clearly verified. Furthermore, investigations of additional reciprocal planes, such as $h0l$, $hk\frac{1}{8}$ planes, etc., confirmed that scattering intensities are found on $\frac{2n+1}{2}\ 0\ \frac{l}{8}$ and $0\,\frac{2n+1}{2}\ \frac{l}{8}$ positions; while no intensities are found on $\frac{4i}{8}$ positions (n,i integer). The same observations have been confirmed for the other R_2PdSi_3 compounds. The investigated single crystals varied in mass from 400 to 2700 mg without any observed effect on the relative intensity of the superstructure reflections. Moreover, the intensities of superstructure reflections do not change from room temperature to low temperatures while the magnetic ordering temperatures are in the range from 20 to 2 K. Thus,

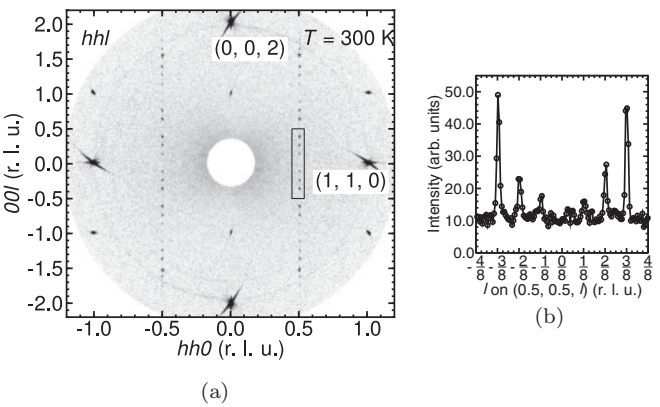

FIG. 3. (Color online) (a) The reciprocal *hhl* plane of Tm_2PdSi_3 measured on E2 at $T = 300$ K and zero field, reproduced from the original 180° scan. (b) The line scan as labeled by the rectangle in the color plot is shown. Additional reflections at $h = k = \pm 0.5$ and $l = \pm\frac{1}{8}, \pm\frac{2}{8}$, and $\pm\frac{3}{8}$ can be identified.

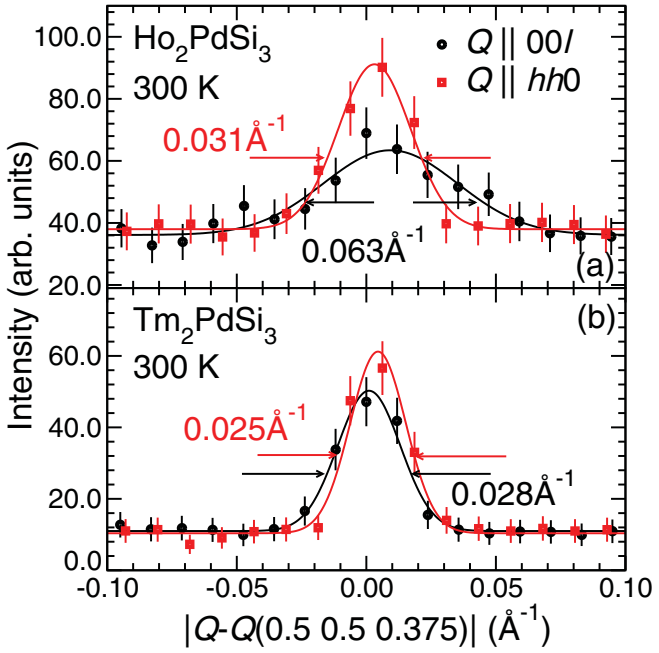

FIG. 4. (Color online) Q scans through the superstructure reflection $\frac{1}{2}\,\frac{1}{2}\,\frac{3}{8}$ of (a) Ho_2PdSi_3 and (b) Tm_2PdSi_3 along different directions in reciprocal space at 300 K.

the superstructure reflections are of crystallographic nature only.

1. Correlation lengths of the superstructure

The correlation lengths of the superstructure vary both in samples and in crystallographic directions. The dependence of the correlation length on the crystallographic direction has been qualitatively observed in x-ray and neutron scattering. To directly compare the variation with samples, the same experimental setup (sample environment, temperature, instrument) is required which has been the case for neutron diffraction measurements on Ho_2PdSi_3 and Tm_2PdSi_3. Figure 4 shows Q scans through the superstructure reflection $\frac{1}{2}\,\frac{1}{2}\,\frac{3}{8}$ in Ho_2PdSi_3 and Tm_2PdSi_3 along different directions in reciprocal space, the latter of which is shown in Fig. 3.

As can be seen for Ho_2PdSi_3 the full width at half maximum (FWHM) along 00l direction (0.063 Å^{-1}) is twice the FWHM along $hh0$ direction (0.031 Å^{-1}). On the other hand, for Tm_2PdSi_3 the FWHM is 0.028 and 0.025 Å^{-1} in 00l and $hh0$ directions, considerably smaller than that for Ho_2PdSi_3.

The angular separation of the multichannel detector on E2 is 0.2° in 2θ; the separation in Q space is then $d(\frac{4\pi}{\lambda}\sin\theta) = \frac{4\pi}{\lambda}\cos\theta d\theta$ which is about 0.017 Å^{-1} at $Q = Q(\frac{1}{2}\,\frac{1}{2}\,\frac{3}{8})$. This is the limit of the instrument resolution. The observed FWHM of a reflection ($FWHM_{obs}$) is determined by the intrinsic FWHM of the reflection ($FWHM_{intr}$) and the instrumental resolution ($FWHM_{RS}$) together:

$$FWHM_{obs} = \sqrt{FWHM_{intr}{}^2 + FWHM_{RS}{}^2}. \qquad (1)$$

We use 0.017 Å^{-1} as an approximate instrumental resolution to estimate the intrinsic FWHM of the structure. This, however, would be an overestimate of the $FWHM_{intr}$ since $FWHM_{RS}$ is definitely larger than 0.017 Å^{-1}. The correlation length (calculated as $\frac{2\pi}{FWHM_{intr}}$) of the superstructure is thus determined to be around 100 Å along 00l direction and 245 Å along $hh0$ direction for Ho_2PdSi_3; 292 and 350 Å in 00l and $hh0$ directions for Tm_2PdSi_3. The correlation length of a main structure reflection (001 in Tm_2PdSi_3) is about 450 Å. Note that the correlation lengths are underestimated due to the overestimated $FWHM_{intr}$.

The difference of the correlations lengths between samples might be due to small differences in the cooling rates during the crystal growth. In this context it should be mentioned that in as-cast polycrystalline samples the superstructure is not detectable, while superstructure reflections are observed in crushed single crystals. The rapid cooling the as-cast samples undergo might lead to a correlation length so small that the reflection intensity is not separated from the background. In general, a larger correlation length of the superstructure has been observed for the basal plane than along the ***c*** direction in all investigated compounds.

C. Summary of the observations

The experimental findings from x-ray and neutron diffraction can be summarized as follows.

(1) Additional crystallographic reflections are observed at $\boldsymbol{Q} = \boldsymbol{G} + \boldsymbol{H}(\frac{1}{2}\ 0\ \frac{i}{8})$, $\boldsymbol{H}(0\ \frac{1}{2}\ \frac{i}{8})$, and $\boldsymbol{H}(\frac{1}{2}\ \frac{1}{2}\ \frac{i}{8})$ where $\boldsymbol{G}$ and $\boldsymbol{H}$ represent reciprocal lattice vectors of main and additional reflections, and $i = \pm1, \pm2$, or ±3. This indicates an enlarged unit cell of the size $2\times2\times8$ of the primitive cell.

(2) No intensities occur at $\boldsymbol{Q} = \boldsymbol{G} + \boldsymbol{H}(0\ 0\ \frac{i}{8})$, which suggests that the scattering power of each scattering plane perpendicular to the ***c*** direction is equivalent to that of the primitive structure, that is, no vacancies or site disorder involving rare earth atoms exist, and the ratio between numbers of Pd and Si atoms on each Pd-Si layer is 1:3.

(3) No intensities are observed at $\frac{4i}{8}$ positions with i being an integer, which suggests that the scattering power along each chain parallel to the ***c*** direction is equivalent to the primitive structure, that is, the ratio between numbers of Pd and Si atoms along each Pd-Si chain is 1:3.

(4) The observed superstructure reflections can be described by the hexagonal Laue symmetry $6/mmm$ with approximately equal intensities of symmetry equivalent reflections.

(5) Neutron and x-ray scattering intensities of the additional reflections are the strongest for reflections with $l = \frac{3}{8}, \frac{5}{8}$, followed by those with $l = \frac{2}{8}, \frac{6}{8}$, and the weakest with $l = \frac{1}{8}, \frac{7}{8}$. The intensity ratio is roughly 4 : 2 : 1 for all compounds. No correlation of the intensity ratio and the rare earth atoms is found, which implies that the superstructure is mainly caused by Pd and Si modulations.

These results indicate that the specific superstructure diffraction pattern is generated by different stacking variants and the question arise if a clear discrimination of these variants is possible.

IV. THEORETICAL MODELING WITH DFT

In the primitive structure the Pd and Si atoms are supposed to be randomly distributed on the 2d sites. However, the occurrence of the superstructure reflections suggests that the random occupancy is replaced by a specific and modulated occupancy

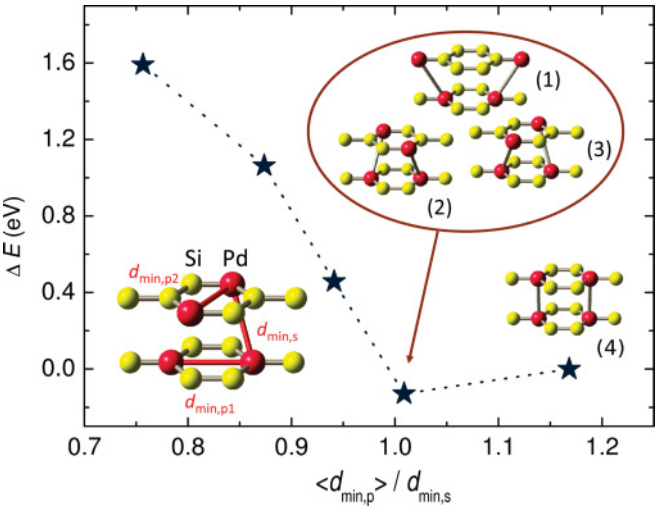

FIG. 5. (Color online) Calculated total energies of different stacking configurations within the hexagonal Ho_2PdSi_3 structure for the volume-optimized cells. The differences are shown with respect to the high-symmetry structure as a function of $\langle d_{\min,p}\rangle/d_{\min,s}$, where $\langle d_{\min,p}\rangle = \frac{d_{\min,1}+d_{\min,2}}{2}$ with $d_{\min,1}$ and $d_{\min,2}$ being the shortest intraplanar Pd-Pd distance in the two neighboring Pd-Si planes, and $d_{\min,s}$ is the shortest interplanar Pd-Pd distance (errors smaller than symbol size). The insets illustrate the simulation cells of the low energy configurations with in-plane as well as Pd-Pd bonds (Si: yellow spheres, Pd: red spheres, Ho: not shown).

on the 2*d* sites. In order to clarify the preferred occupancy of mixed Pd/Si sites in the structure, possible hexagonal stacking configurations, as shown in Fig. 5, were investigated by calculations with gradient-corrected density functional theory (DFT). As the experiments indicate that the additional reflections are of crystallographic origin, magnetic ordering in the stacks was suppressed and spin-polarization omitted. The projector-augmented wave (PAW) method[50] (in Perdew-Wang parametrization[51]) was employed as implemented in the VASP code.[52] Total energies have been converged (better than 10^{-8} eV) with a maximum kinetic energy of 450 eV for the plane wave basis set (700 eV for the augmentation charges) and a k-point grid equivalent to a $12 \times 12 \times 12$ Monkhorst-Pack grid for the $8.0994 \times 8.0994 \times 8.0048$ Å^3 hexagonal cell. Increasing the k mesh to $18 \times 18 \times 18$ grid points yielded a total energy change below 1 meV. The tetrahedron method with Blöchl corrections was applied. All structures have been fully relaxed with respect to atomic positions. Cell geometry was treated in two different approaches. First, the cell was fixed to the experimental parameters and second, an isotropic volume relaxation was considered and all positions were relaxed within the space group.

The total energies of the hexagonal stacking configurations have been calculated and are compared in Fig. 5 for the volume-optimized case. It can be seen that the three symmetry equivalent configurations (1–3) exhibit the lowest total energy and are favorable with respect to all other configurations, even the high-symmetry case (4) with an energy difference of approximate 0.13 eV. Configurations corresponding to smaller Pd-Pd distances are found to be energetically unfavorable and thus improbable to be encountered. The energies for the experimental cells show an equivalent tendency with a slight total energy increase of about 0.02 eV due to strains of less than 0.8%. Relaxations amount to less than 0.04 Å for the low energy structures (1–4) and to less than 0.13 Å for the other configurations.

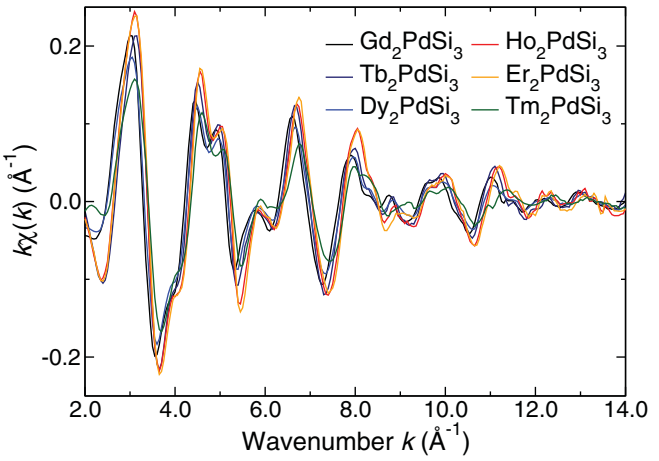

FIG. 6. (Color online) The extracted EXAFS function $k\chi(k)$ of the Pd K absorption edge of the R_2PdSi_3 compounds.

Therefore, from the viewpoint of theoretical modeling, random occupancy on the Pd-Si sites is improbable since three configurations [1–3 (Fig. 5)] are energetically favored. On the other hand, it seems likely that the structural modulation results from the stacking of the three symmetry-equivalent and therefore degenerate configurations.

V. CHARACTERIZATION OF THE LOCAL STRUCTURE: EXAFS

In order to verify the DFT results, the local structure of the Pd, Si, and R atoms is inspected by EXAFS. Theoretical calculations by McKale *et al.*[53] have shown that the scattering data of Si or Pd atoms can be well distinguished, which makes it possible to test different atomic environments of the specific absorbing atom, that is, Pd or R.

A. Pd *K* EXAFS

In Fig. 6 the Pd K EXAFS data of the R_2PdSi_3 (R = Gd, Tb, Dy, Ho, Er, Tm) powder samples are shown. Despite the fact that only the Ho_2PdSi_3 and Er_2PdSi_3 samples were prepared from single crystalline materials, the individual curves, which are shown in Fig. 6, exhibit comparable features pointing to an almost identical local atomic structure. Therefore, the local structure around the Pd atom is an intrinsic property and the same for all the investigated R_2PdSi_3 compounds.

Hereafter, data evaluation of the Ho_2PdSi_3 compound is performed as an example, but results and interpretations apply to the other investigated compounds as well. The direct neighborhood (first coordination sphere) of the Pd atoms was first investigated to fit the observed EXAFS data. Different atomic environments were tested and the results are shown in Fig. 7. The most probable atomic environment of the Pd atoms is with three Si atoms as nearest neighbors (model 1: final residual R = 6.38%, orange line in Fig. 7). Replacing Si with Pd atoms in the direct neighborhood leads to significantly worse residuals: R = 18.71% (model 2) and R = 13.22%

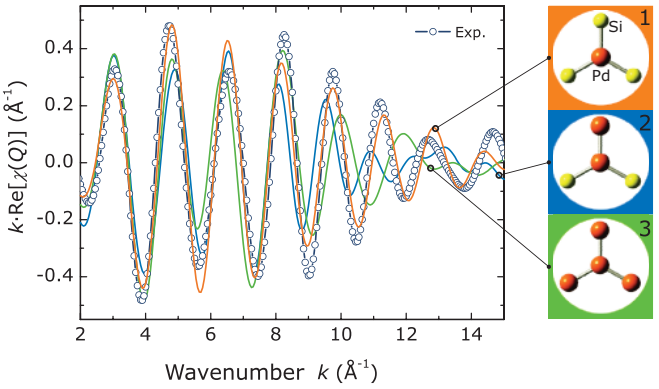

FIG. 7. (Color online) Results of fitting three models to the experimental Pd K EXAFS data $k\mathrm{Re}\,\chi(Q)$ of Ho_2PdSi_3 (black circles). Exclusively the first coordination sphere ($r_{max} = 2.4$ Å) of the Pd atoms was investigated. The three models are shown on the right: model 1 (three Si neighbors: orange line), model 2 (two Si neighbors: blue line), and model 3 (three Pd neighbors: green line).

(model 3). Additionally, a mean environment or a potential disorder was tested by refining a combination of models 1 and 3. As a result, nonphysical parameters and strongly enhanced standard deviations of all refined parameters were obtained so that such a model can be excluded. This agrees well with the DFT calculation and its three favored configurations where small Pd-Pd distances are found to be unstable (cf. Fig. 5).

B. Rare earth-L EXAFS

As suggested by the diffraction measurements, the unit cell of the Ho_2PdSi_3 is enlarged by factor $2 \times 2 \times 8$ which results in the possibility of multiple, nonequivalent R sites. These different sites should be distinguishable with respect to their electronic surrounding. To address this question, the R L EXAFS functions were analyzed. In Fig. 8 the Ho and Er L EXAFS functions are shown. The R L EXAFS data are nearly identical for these two compounds as well as for R = Tb (not shown). In the following, only the data for Ho_2PdSi_3 will be discussed but the conclusions should be valid for all R_2PdSi_3 compounds.

The DFT calculation yielded three symmetry equivalent configurations which are energetically favored. These three configurations are comprised of two possibilities for the local structure of the rare earth atoms (R_1, R_2). The nearest neighbors of the rare earth atoms are 12 Pd/Si atoms in two rings arranged above and below the rare earth atoms. For R_1 one of the rings consists only of Si atoms, the other one of two Pd and four Si atoms. For R_2 both rings are comprised of two Pd and four Si atoms [see Fig. 9(b)].

For the EXAFS analysis both cluster models have to be superimposed because both R atoms (R_1 and R_2) act as absorbing atoms at the same time. Therefore, it is not possible to directly determine the local structure of a single R atom only. Furthermore, there are no differences between signals from the two configurations, when only single scattering paths with $r_{max} < 3.1$ Å are taken into account, since the EXAFS method uses only lengths of the scattering paths but not the angles between them. Nevertheless, certain coordination information can be obtained and are described in the following.

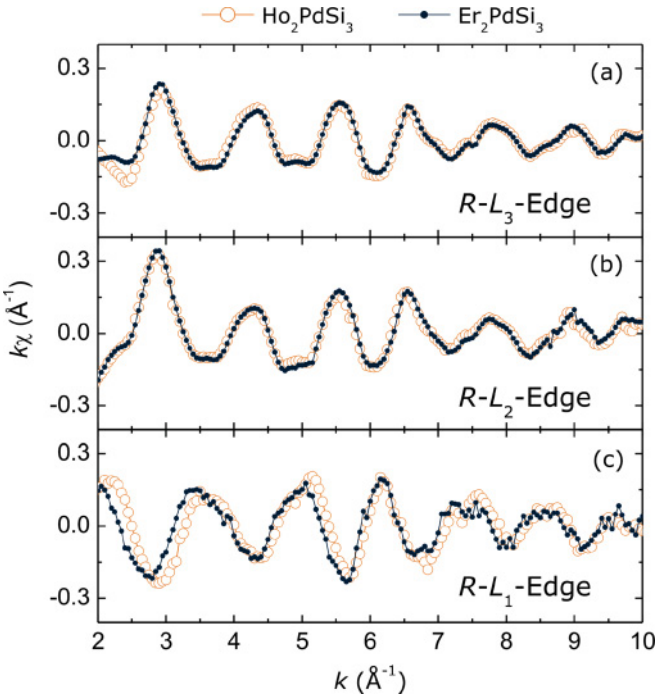

FIG. 8. (Color online) The extracted EXAFS functions $k\chi(k)$ of the Ho and Er L absorption edge of Ho_2PdSi_3 (orange) and Er_2PdSi_3 (blue) compounds, respectively.

The experimental data were first fitted using an atom cluster with $r_{max} = 3.1$ Å and single scattering paths. The model with a combination of atom clusters with either only Si as nearest neighbors or only Pd as nearest neighbors fits the data at best. A fraction of 78(11) at. % Si and 22(8) at. % Pd could be estimated. This agrees well with the suggested ideal composition of 3:1 (Si:Pd).

Second, an atom cluster with $r_{max} = 6.0$ Å and multiple scattering paths from the two different surroundings were generated and refined. The fitting results for the Ho L_3 EXAFS data are depicted in Fig. 9(a).

As can be seen, the experimental data are well reproduced, which proves the predictions of the DFT calculations that only two different atomic surroundings of the R atoms occur.

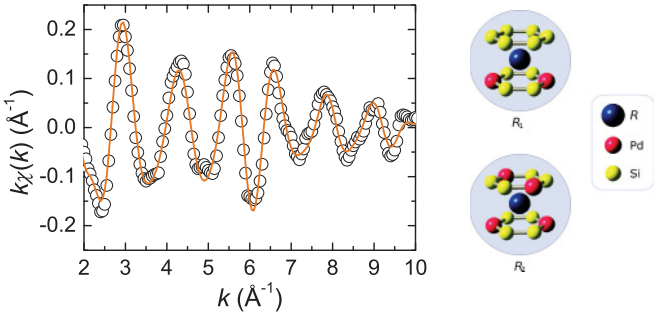

FIG. 9. (Color online) Ho L_3 EXAFS data and simulated curves for different cluster models. (a) Refinement results for a cluster with $r_{max} = 6.0$ Å. Shown here is the simulated curve $k\chi(k)$ for a model comprising of both R sites (R = 1.58%). (b) The two possibilities of the first coordination sphere of the two symmetrically not equivalent rare earth atoms (for details see text).

C. Summary

From quantitative EXAFS analysis the following conclusions can be drawn.

(1) All investigated R_2PdSi_3 samples exhibit an identical local structure for the Pd as well as for the R atoms.

(2) The first coordination sphere of the Pd atoms consists of three Si atoms.

(3) For the rare earth atoms two different surroundings R_1, R_2 exist.

VI. THE SUPERSTRUCTURE MODEL

Based on the x-ray and neutron diffraction results, EXAFS data and DFT calculation, a structure model is proposed to describe the superstructure observed in R_2PdSi_3. The model uses a modulation wave approach in which the structure is described as superposition of an average structure and a set of modulated structures.[54–56] In general the modulation can be occupational, positional, or a combination of both. The possible solutions are analyzed with the means of group theory which yields a unique structure solution.

Based on the experimental observations, the following assumptions are made to simplify the structure model.

(1) The superstructure is due to the Pd-Si modulation, based on the diffraction measurements where the relative intensities of the superstructure reflections is independent of R.

(2) The Wyckoff $2d$ sites are occupied by either Pd or Si. As shown by DFT calculations and verified by EXAFS, there are three configurations which are energetically favored. A random occupancy is therefore unlikely.

(3) The Pd-Si modulation is of occupational nature as verified by DFT calculation. The possible positional modulations are below 0.1 Å (rare earth atoms) and 0.01 Å (Si/Pd atoms) based on x-ray diffraction data. The positional modulation will be used in the later refinement as a free parameter.

The intensity of the superstructure reflections depends then only on the scattering length $b_{p=1,2}(\boldsymbol{X})$ where the index p denotes the positions $\boldsymbol{r}_1$ and $\boldsymbol{r}_2$ in the main unit cell. $b_{p=1,2}(\boldsymbol{X})$ can be decomposed into an average part and a modulated part.

$$
\begin{aligned}
b_{p=1,2}(\boldsymbol{X}) &= \frac{3b_{\mathrm{Si}} + b_{\mathrm{Pd}}}{4} + \delta b_p(\boldsymbol{X}) \\
\text{with } \delta b_p(\boldsymbol{X}) &= \sum_{q=1,2,3} b_{\boldsymbol{\tau}_1^q,p} e^{i2\pi\boldsymbol{\tau}_1^q\cdot\boldsymbol{X}} \\
&\quad + \sum_{q=1,2,3} b_{\boldsymbol{\tau}_2^q,p} e^{i2\pi\boldsymbol{\tau}_2^q\cdot\boldsymbol{X}} \\
&\quad + \sum_{q=1,2,3} b_{\boldsymbol{\tau}_3^q,p} e^{i2\pi\boldsymbol{\tau}_3^q\cdot\boldsymbol{X}} + \text{c.c.} \qquad (2)
\end{aligned}
$$

with the modulation vectors $\boldsymbol{\tau}_{s=1,2,3}^q$ and the Fourier components $b_{\boldsymbol{\tau},p}$ for each modulation vector. The superstructure model is equivalent with the determination of these Fourier components which is presented in the following.

Recall from Sec. II that the sequence along $\boldsymbol{c}$ on one Pd/Si site ($\boldsymbol{r}_1$ or $\boldsymbol{r}_2$) can only consist of six Si and two Pd atoms in the enlarged unit cell. Also, no intensities are found on $l = \frac{0}{8}$ and $l = \frac{4}{8}$ positions. After enumeration of all possibilities the latter condition is fulfilled by only two possible sequences: sequence 1 Pd-Pd-Si-Si-Si-Si-Si-Si and sequence 2 Pd-Si-Si-Pd-Si-Si-Si-Si. Only the latter is in agreement with both DFT calculation and EXAFS measurements since in sequence 1 there are two Pd atoms neighboring each other in $\boldsymbol{c}$ direction.

TABLE III. Fourier components for modulation vectors $b_{\boldsymbol{\tau}}$ of the crystallographic superstructure, where $b^q = c_q^2 \frac{b_{\mathrm{Si}}-b_{\mathrm{Pd}}}{4} e^{i\phi_q^2}$; the exact values for c_q^2 and ϕ_q^2 are listed in Table VIII.

q	1	2	3
$b_{\boldsymbol{\tau}_1^q}$	$\frac{\sqrt{2}}{2}b^1 e^{-i\frac{\pi}{4}}$	0	$\frac{\sqrt{2}}{2}b^3 e^{i\frac{\pi}{4}}$
$b_{\boldsymbol{\tau}_2^q}$	$\frac{\sqrt{2}}{2}b^1 e^{i\frac{\pi}{4}}$	0	$\frac{\sqrt{2}}{2}b^3 e^{-i\frac{\pi}{4}}$
$b_{\boldsymbol{\tau}_3^q}$	0	b^2	0

While the sequence on one of the Pd/Si sites is thus determined, the phase shift of the sequence between $\boldsymbol{r}_1$ and $\boldsymbol{r}_2$ can assume eight possible values, i.e., 0, $\frac{2\pi}{8}$, ..., $7\cdot\frac{2\pi}{8}$. This leads in principle to $(2\times 8)^8$ possible structures (8 in the power corresponds to the eight Pd/Si sites in the enlarged unit cell).

However, following the analysis in Appendix A, only four possible solutions which are in agreement with the experimental results exits in total. Among them only one is consistent with sequence 2. To express the result in the basic unit cell, the modulation vectors are categorized into three classes: $\{\pm\boldsymbol{\tau}_1^q\} = \{\pm(\frac{1}{2}\ 0\ \frac{q}{8})\}$, $\{\pm\boldsymbol{\tau}_2^q\} = \{\pm(0\ \frac{1}{2}\ \frac{q}{8})\}$, and $\{\pm\boldsymbol{\tau}_3^q\} = \{\pm(\frac{1}{2}\ \frac{1}{2}\ \frac{q}{8})\}$. The Fourier components of the modulation vectors for this solution are listed in Table III.

So far the relation between the two Pd/Si sites in the basic unit cell has not been discussed. However, symmetry of the basic structure prescribed a certain limit, so that the Fourier components of the two sites, that is, $b_{\boldsymbol{\tau},1}$ and $b_{\boldsymbol{\tau},2}$, are not independent. For example, applying $P6/mmm$ symmetry to the modulation vector $\boldsymbol{\tau}_1^1$, the small group that leaves the modulation vector unchanged consists of four symmetry elements $G_{\boldsymbol{\tau}_1^1} = \{1,\ 2_{0,0,z},\ \mathrm{m}_{2x,x,z},\ \mathrm{m}_{0,y,z}\}$. There are four irreducible representations of the group, the character table for which are given in Table IV. The basis functions can be constructed using $b_{\boldsymbol{\tau},1}$ and $b_{\boldsymbol{\tau},2}$ for each representation as listed in Table IV.

Although the small groups are comprised of different symmetry elements for different modulation vectors, they are isomorphic to each other, and also to the factor group of the subgroup $D_3 = \{1, 3^-_{0,0,z}, 3^+_{0,0,z}, 2_{x,x,0}, 2_{0,y,0}, 2_{x,0,0}\}$ of $P6/mmm$. Following the analysis in Appendix B, it is

TABLE IV. The character table for the irreducible representations of the small group G_τ of modulation vector $\boldsymbol{\tau}_1^1 = (\frac{1}{2}0\frac{1}{8})$ in space group $P6/mmm$. The basis functions are constructed with the Fourier components of the modulation vector on each site $b_{\boldsymbol{\tau},1}$ and $b_{\boldsymbol{\tau},2}$ when possible.

	1	$2_{0,0,z}$	$\mathrm{m}_{2x,x,z}$	$\mathrm{m}_{0,y,z}$	Basis
Γ^1	1	1	1	1	$b_{\boldsymbol{\tau},1} + b_{\boldsymbol{\tau},2}$
Γ^2	1	1	−1	−1	
Γ^3	1	−1	1	−1	$b_{\boldsymbol{\tau},1} - b_{\boldsymbol{\tau},2}$
Γ^4	1	−1	−1	1	

TABLE V. Taking the space group symmetry $P6/mmm$ into account six superstructure domains occur. Each domain contributes to the intensity of modulation vectors associated to itself.

Domains	$\boldsymbol{\tau}_s^q$ $(0.5, 0.0, \frac{q}{8})$	$(0.0, 0.5, \frac{q}{8})$	$(0.5, 0.5, \frac{q}{8})$
$D_1 = 1 \cdot D_1$	$(0.5, 0.0, \frac{q}{8})$	$(0.0, 0.5, \frac{q}{8})$	$(0.5, 0.5, \frac{q}{8})$
$D_1' = 2_{x,x,0} D_1$	$(0.0, 0.5, -\frac{q}{8})$	$(0.5, 0.0, -\frac{q}{8})$	$(0.5, 0.5, -\frac{q}{8})$
$D_2 = 3^-_{0,0,z} D_1$	$(-0.5, 0.5, \frac{q}{8})$	$(-0.5, 0.0, \frac{q}{8})$	$(-1.0, 0.5, \frac{q}{8})$
$D_2' = 2_{0,y,0} D_1$	$(-0.5, 0.0, -\frac{q}{8})$	$(-0.5, 0.5, -\frac{q}{8})$	$(-1.0, 0.5, -\frac{q}{8})$
$D_3 = 3^+_{0,0,z} D_1$	$(0.0, -0.5, \frac{q}{8})$	$(0.5, -0.5, \frac{q}{8})$	$(0.5, -1.0, \frac{q}{8})$
$D_3' = 2_{x,0,0} D_1$	$(0.5, -0.5, -\frac{q}{8})$	$(0.0, -0.5, -\frac{q}{8})$	$(0.5, -1.0, -\frac{q}{8})$

determined that only a phase shift of π between $b_{\boldsymbol{\tau}_1^1,1}$ and $b_{\boldsymbol{\tau}_1^1,2}$ agrees with the experimental observations.

So far a set of modulation vectors with corresponding Fourier components in Table III which can describe the superstructure in R_2PdSi_3 is found. According to the model, the relations between the two sites $\boldsymbol{r}_1$ and $\boldsymbol{r}_2$ are $b_{\boldsymbol{\tau}_1^1,1} = -b_{\boldsymbol{\tau}_1^1,2}$, $b_{\boldsymbol{\tau}_1^2,1} = b_{\boldsymbol{\tau}_1^2,2}$ and $b_{\boldsymbol{\tau}_1^3,1} = -b_{\boldsymbol{\tau}_1^3,2}$, etc.

The application of the $P6/mmm$ symmetry on the modulation vectors leads to the generation of six twinned domains. They can be transformed into each other with symmetry operations in the subgroup D_3 as shown in Table V.

While each domain has the reduced twofold symmetry (there is only a twofold rotational axis in each of the small groups), the experimentally observed quasihexagonal structure is due to an average of the six twinning domains. Although $b_{\boldsymbol{\tau}_3^1} = 0$ for domain D_1 (see Tables III and V), there are still observed intensities on this position due to contributions from domain D_3, D_3', D_2, and D_2'. Similarly, all other observed superstructure reflections can be considered as an averaged contribution from the six domains. The ratio between the square of the structure factors of the $\frac{1}{8}$, $\frac{2}{8}$, and $\frac{3}{8}$ reflections is 1:3.4:5.8, depending only on the difference between the neutron scattering length of Pd and Si atoms $|b_{Pd} - b_{Si}|^2$. With respect to the experiment uncertainty this ratio is found in all investigated R_2PdSi_3. Other possibilities (e.g., sequence 1) yield ratios which are incompatible with the observed intensities.[27]

A. The superstructure in real space

In real space the superstructure can be constructed by stacking the Pd-Si layers in the $\boldsymbol{c}$ direction. The phase relation leads to four kinds of Pd-Si layers (labeled as A, B, C, and D) allowed in the superstructure as shown in Fig. 10, all of which still preserve the twofold rotational symmetry.

Thus domain D_1 can be translated into the sequence ABCDBADC and is plotted in Fig. 11.

Other symmetrically equivalent domains are of the following arrangements in $\boldsymbol{c}$ direction:

(1) D_1: ABCDBADC; D_1': ABDCBACD
(2) D_2: DBCABDAC; D_2': DBACBDCA
(3) D_3: CBDABCAD; D_3': CBADBCDA

It is worth noting that in the superstructure there are only six combinations between adjacent Pd-Si layers and all of them are symmetrically equivalent to the three configurations with lowest energy as shown in Fig. 5. There are no identical layers

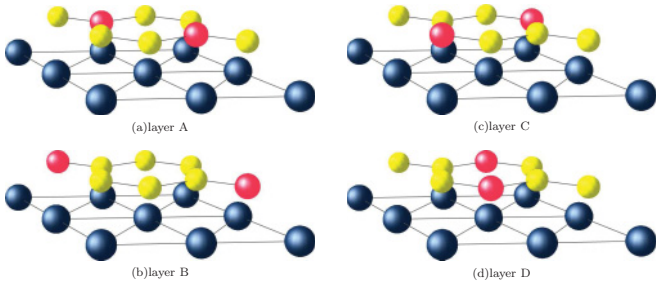

FIG. 10. (Color online) Sketches of the four kinds of Pd-Si layers labeled (a) A, (b) B, (c) C, and (d) D. The rare earth atoms are depicted in blue. The position of the silicon (yellow) and palladium (red) atoms is $c/2$ above the rare earth plane.

which are adjacent to each other in the sequences. This again agrees well with the DFT calculations which showed that such a configuration (4 in Fig. 5) is energetically unstable. Also it is to be recalled that there are only two types of local structures for rare earth atoms as shown in Fig. 9(b).

In other terms, the sequence of layers in the enlarged unit cell can be understood as a sequence of rotations and translations of any Pd-Si layer. It is easily seen that the layers A, C, and D are transferred to each other by a 60° rotation. The counterclockwise rotation is defined $\mathcal{R}$, the clockwise $\bar{\mathcal{R}}$. The B layer is invariant under $\mathcal{R}$ and $\bar{\mathcal{R}}$. Each layer A, C, and D has an in-plane twofold axis. The translation with the primitive lattice vector $\boldsymbol{a}$ along the respective twofold axis of A, C, and D leads to layer B and vice versa. The translation is defined T_{110}, T_{010}, and T_{100} with the subscript for the twofold axis of the respective layer A, C, and D. It is obvious that T_{110} is transformed to T_{010} by a $\mathcal{R}$ operation, and so on. With this notion, all superstructure domains can be described with one sequence of operations on different starting layers, which is T - $\mathcal{R} \cdot T$ - $\mathcal{R}$ - $\mathcal{R} \cdot T$ - $\mathcal{R} \cdot T$ - $\mathcal{R}$ - $\mathcal{R}$ with T in the direction of the twofold axis of the current layer. This can be understood as a three times counterclockwise rotation with two translations and two clockwise rotations. For example, the domain D_1 is realized by applying the following operations on layer A: T_{110} - $\mathcal{R} \cdot T_{110}$ - $\mathcal{R}$ - $\mathcal{R} \cdot T_{010}$ - $\mathcal{R} \cdot T_{100}$ - $\mathcal{R}$ - $\mathcal{R}$. The D' domains are found by exchanging $\mathcal{R}$ and $\bar{\mathcal{R}}$.

B. Refinement of the superstructure model

The intensities of the superstructure reflections from neutron scattering are rather weak and the number of available reflections is too small to examine quantitatively the validity of the model. Therefore, although x-ray diffraction data is only available for Ho_2PdSi_3, it (instead of the neutron scattering data for a larger collection of R_2PdSi_3 compounds) is used for comparison with the model calculation. Due to the similarity shown in the neutron scattering data of the different R_2PdSi_3 compounds, it is expected that this will not compromize the validity of the model.

During the course of refinement, the lattice parameters are fitted first and then held constant. The atom positions in the enlarged unit cell are fixed according to the model described in the previous section. Randomly but equally distributed twinned domains are assumed so that contributions from different domains are simply summed up. Initially, only scaling

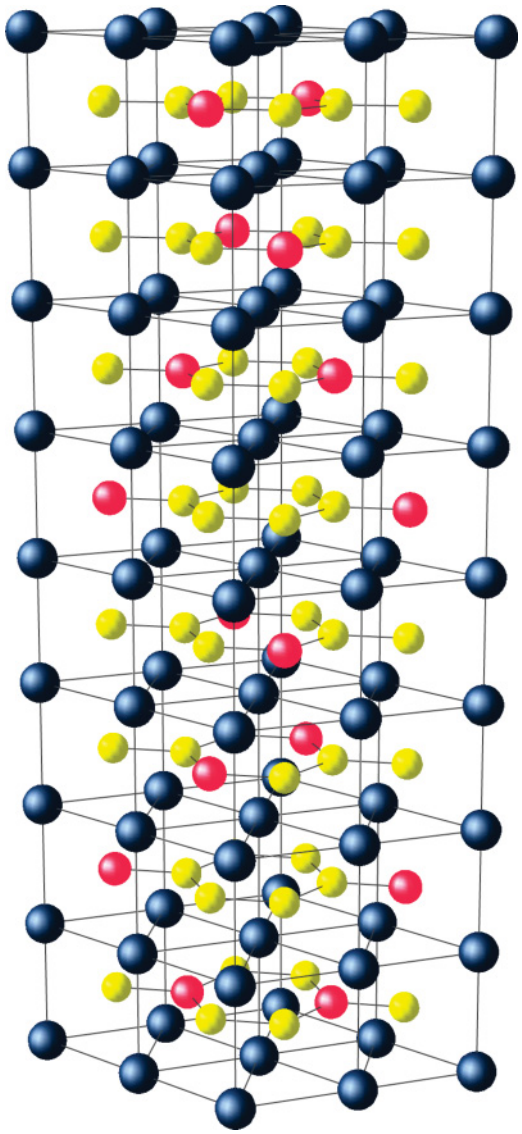

FIG. 11. (Color online) Sketch of superstructure D_1 of the layer sequence ABCDBADC.

and extinction factors are refined. The obtained R values were around 20% for the superstructure reflections in the beginning when all atomic positions are fixed. However, considering the two types of local structures for Ho (see right side of Fig. 9), the R_1 type atom is probably pushed away from the Pd atoms (radius ∼1.4 Å) to the other side where there are only Si atoms (radius ∼1.1 Å). On the other hand, the R_2 type atom is probably in the original position since there are Pd atoms on both sides. Putting this assumption into the model and refining three parameters (scaling, extinction, and the atomic displacement of the Ho^{3+} atoms in R_1 positions) in total, the R values dropped to around 11% with a displacement of the Ho^{3+} atoms in R_1 positions of 0.026 Å.

Details of the refinement and R values are summarized in Table VI. For comparison, results from refinement with another model are also listed in Table VI, details for the second model can be found elsewhere.[27,37,41] The second model describes the superstructure by a modulation approach using a modulation vector $\boldsymbol{\tau} = (00\frac{3}{8})$ and an enlarged unit cell $2a \times 2a \times c$ with space group symmetry $P6/mmm$. Assuming both occupational and positional modulations, considering symmetry requirements, 30 independent parameters were refined. As shown in Table VI, the R factors are comparable but slightly larger than the current model.

In summary, the current superstructure model agrees well with the Ho_2PdSi_3 data. Although the R factors of the second model are comparable with the current one, the physical picture of the current model is simpler. Moreover, the current model fits better into the picture when the magnetic structures are involved.

VII. DISCUSSIONS

A. Crystallographic structure

To summarize, the superstructure observed in R_2PdSi_3 can be described using the modulation vectors with the respective Fourier components tabulated in Table III. In the real structure the symmetry reduction from the $P6/mmm$ symmetry of the main structure leads to the existence of six twinned domains. The averaged diffraction picture is therefore quasihexagonal. The combination of neutron and x-ray diffraction measurements allowed the separation of other possible effect for the observed diffraction pattern. The structure of the bulk measured by neutrons allowed us to falsify a possible surface ordering while the single crystal x-ray measurement excluded a possible co-aligned parasitic phase. The neutron diffraction showed the same characteristic 1:2:4 intensity pattern for $\frac{1}{8}$, $\frac{2}{8}$, $\frac{3}{8}$ reflections for all investigated R_2PdSi_3. This intensity pattern is specific here for the presented structure proposal and cannot be reproduced by other stacking sequences. Additionally, neutron diffraction allowed us to investigate a possible change of the superstructure reflection from room temperature through the magnetic ordering down to 1.5 K. No change was observed. The superstructure is therefore not influenced by the magnetic rare earth ions, but the influence of the superstructure on the magnetic properties are significant as will discussed in the next subsection.

The refinement of the model with x-ray diffraction data of the Ho_2PdSi_3 compound yielded a $w\mathrm{R}_{F^2}$ factor of 11.35% for the superstructure reflections, best among all other tested possibilities. It is interesting to note that the refinement of all reflections in the main structure model (where the superstructure reflections are deviations) yields a $w\mathrm{R}_{F^2}$ factor of about 12.5%. The intensity of the superstructure reflections is proportional to the difference of the scattering lengths and therefore small in comparison to the main structure reflections. The fact has to be considered when a classic structure solution with a x-ray diffraction pattern is refined. The refinement leads easily to a dead-end due to the insignificance of the superstructure reflections for the fit.

The combination of diffraction measurements with DFT calculations and EXAFS measurements indicated the existence of only two kinds of local environments for rare earth atoms. This can be interpreted in the light that Pd atoms avoid each other as nearest neighbors due to their size. Furthermore, DFT calculations showed that stacking sequences of lowest energy exist compared to other possible sequences where identical layers (i.e., Pd atoms) are adjacent to each other.

TABLE VI. Crystallographic data and details of the structure refinement. The R values are given for the observed and for all reflections (observed/all).

Chemical formula	Ho_2PdSi_3	
Cell parameter[b]	$a = b = 4.0497(3)$ Å, $c = 4.0024(3)$ Å	
	$\alpha = \beta = 90°$, $\gamma = 120°$	
Refinement on	F^2	
Extinction correction	isotropic, Lorentz	
	Current Model	Other Model
Number of refined parameters[b]	3	30
Weighted R values[43]		
$wR_{F^2,\text{all}}$ (obs./all)	9.38% / 11.45%	12.88% / 19.16%
$wR_{F^2,\text{main}}$ (obs./all)	8.60% / 8.82%	12.06% / 12.88%
$wR_{F^2,\text{sup.}}$ (obs./all)	11.35% / 14.23%	n/a
Goodness of fit (obs./all)	3.30 / 1.73	3.24 / 1.92

[b]Cell parameters of AlB_2-equivalent unit cell.
[b]The superstructure cell consists of 96 atoms in total, which needs 288 parameters to fully specify the structure when no model is assumed.

In real space the superstructure can be described as six stacking sequences ABCDBADC, etc. of the different layers along the ***c*** direction. The sequence includes a rotation from layer to layer. Additionally, a translation along the twofold axis of a layer with a primitive lattice vector ***a*** seems energetically favored. The delicate stacking sequence can be thermally influenced as the findings of different correlation lengths imply stacking faults along the ***c*** direction. The detailed investigation of the conditions for the superstructure formation (for instance through an *in situ* diffraction experiment while annealing a powder sample) is beyond the scope of this paper. The domain size is about several hundred Ångstrom as suggested by the calculation of the correlation lengths based on the measured FWHM. In some compounds, like Ho_2PdSi_3, the correlation length is about half of that in the basal plane, which indicates that the stacking faults occur preferably along the ***c*** direction. This is an expected behavior for the so called type B order-disorder structures introduced by Dornberger-Schiff.[57] The finding of the stacking faults might well explain the contradictory literature data on the crystallographic structure of R_2PdSi_3 and related compounds.

The superstructure is not specific to the single crystal case. The EXAFS data have shown that also in polycrystalline samples only two surroundings for the rare-earth atoms exist. It is suggested that the powder samples are so heavily disordered that the correlation length is actually below the size of the structural unit cell. In Ce_2PdSi_3 it has been shown that superstructure reflections have been observed after a week of annealing also in polycrystalline samples.[29]

Interestingly, the network of the rare-earth atoms still remains in the primitive AlB_2 structure with only a slight indication of displacement and no site defects (vacancies or occupation by Pd/Si atoms). Opposed to the assumption of Chevalier *et al.*[8] the formation of Si-Hueckel arenes proves to be stable against increasing electron number of the *d*-shell electrons in the transition metal. Instead the transition metal is incorporated in the Si network and the increasing size of the transition metal ion (from Ru over Rh to Pd) leads to the introduction of a longer stacking sequences along the ***c*** direction. In the light of the stability of the Si-Hueckel arenes and the delicate dependence on sample preparation the findings on other R_2TSi_3 compounds where diffuse intensity has been observed on $\frac{1}{2}\frac{1}{2}l$ positions might be re-interpreted.

B. Implications for the magnetic properties

The crystallographic superstructure has an eminent impact on the magnetic properties of the R_2PdSi_3 compounds. In the so called FiM phase[38] of Ho_2PdSi_3 and Tb_2PdSi_3, magnetic intensities were observed on top of the superstructure reflections when a magnetic field was applied on the sample. The existence of the FiM phase has been also confirmed for Er_2PdSi_3 and Tm_2PdSi_3.[58] In Tm_2PdSi_3[58] magnetic Bragg reflections were observed as satellites to the superstructure reflections.

The superstructure model discussed here provides a new angle to tackle the correlation between the magnetic structure and the crystallographic superstructure. As discussed before, two different local environments for R^{3+} atoms exist. That this difference exists and is significant has been shown in the case of Er_2PdSi_3.[59] In the magnetic ordered phase this gives rise to two magnetic sublattices which in themselves can be ordered antiferromagnetically. The FiM phase emerges when these sublattices exhibit different ferromagnetic contributions. Whether these differences are due to crystal electrical field (CEF) effect or RKKY exchange interactions or both cannot be easily decided.[60] In some investigated cases the existence of magnetic domains complicates the analysis further.[61]

However, it is easy to show that the here presented superstructure generates the observed intensity pattern of the FiM although the mechanism is unknown. It is sufficient to start with two types of rare earth atoms (R_1 and R_2).

For a certain crystallographic domain (see Sec. V), the sequence of the rare earth atoms along the ***c*** direction is determined. Using the D_1 domain as an example, the sequences of rare earth atoms at the following positions are as listed below:

(1) $\boldsymbol{X} = (0,0,z)$: R_1-R_2-R_1-R_1-R_2-R_2-R_2-R_1,
(2) $\boldsymbol{X} = (1,0,z)$: R_2-R_1-R_1-R_2-R_1-R_1-R_2-R_2,
(3) $\boldsymbol{X} = (1,1,z)$: R_2-R_2-R_2-R_1-R_1-R_2-R_1-R_1,
(4) $\boldsymbol{X} = (0,1,z)$: R_1-R_1-R_2-R_2-R_2-R_1-R_1-R_2.

Let the ferromagnetic component of the magnetic moments for R_1 and R_2 be $\boldsymbol{\mu}_1$ and $\boldsymbol{\mu}_2$, respectively. Then, the magnetic

TABLE VII. Tabulated Fourier components for modulation vectors $\boldsymbol{\mu}_{\boldsymbol{\tau}}$ of the magnetic structure as the result of the crystallographic superstructure, where $\boldsymbol{\mu}^q = c_q \frac{\boldsymbol{\mu}_1 - \boldsymbol{\mu}_2}{2}$, $c_1 = -c_3 = 2.828427$, and $c_2 = -4$.

q	1	2	3
$\boldsymbol{\mu}_{\boldsymbol{\tau}_1^q}$	$\frac{\sqrt{2}}{2}\boldsymbol{\mu}^1 e^{-i\frac{\pi}{4}}$	0	$\frac{\sqrt{2}}{2}\boldsymbol{\mu}^3 e^{i\frac{\pi}{4}}$
$\boldsymbol{\mu}_{\boldsymbol{\tau}_2^q}$	$\frac{\sqrt{2}}{2}\boldsymbol{\mu}^1 e^{i\frac{\pi}{4}}$	0	$\frac{\sqrt{2}}{2}\boldsymbol{\mu}^3 e^{-i\frac{\pi}{4}}$
$\boldsymbol{\mu}_{\boldsymbol{\tau}_3^q}$	0	$\boldsymbol{\mu}^2$	0

moment of the rare earth atom in the $\boldsymbol{X}$th position can be described using the Fourier transformation as follows:

$$\begin{aligned}\boldsymbol{\mu}(\boldsymbol{X}) &= \frac{\boldsymbol{\mu}_1 + \boldsymbol{\mu}_2}{2} + \delta\boldsymbol{\mu}(\boldsymbol{X}) \\ \text{with } \delta\boldsymbol{\mu}(\boldsymbol{X}) &= \sum_{q=1,2,3} \boldsymbol{\mu}_{\boldsymbol{\tau}_1^q} e^{i2\pi\boldsymbol{\tau}_1^q\cdot\boldsymbol{X}} \\ &+ \sum_{q=1,2,3} \boldsymbol{\mu}_{\boldsymbol{\tau}_2^q} e^{i2\pi\boldsymbol{\tau}_2^q\cdot\boldsymbol{X}} \\ &+ \sum_{q=1,2,3} \boldsymbol{\mu}_{\boldsymbol{\tau}_3^q} e^{i2\pi\boldsymbol{\tau}_3^q\cdot\boldsymbol{X}} + \text{c.c.} \end{aligned} \quad (3)$$

The Fourier components for each modulation vector $\boldsymbol{\tau}_s^q$ are listed below in the Table VII. The crystallographic superstructure naturally induces possible magnetic structures with the same modulation vectors $\boldsymbol{\tau}_s^q$ when the ferromagnetic component of the magnetic moments $\boldsymbol{\mu}_1$ and $\boldsymbol{\mu}_2$ are not equal and nonzero. The magnetic intensity pattern on the superstructure reflections is roughly 1:2:1 for $\frac{1}{8}$, $\frac{2}{8}$, and $\frac{3}{8}$. This is exactly what has been observed in the FiM phase where the difference between $\boldsymbol{\mu}_1$ and $\boldsymbol{\mu}_2$ is induced by external fields.

The influence of the crystallographic superstructure on the magnetic structures depends on how strongly the rare earth atoms are influenced by the different local environments. If we consider the CEF effect only, the influence for the Gd^{3+} atom should be weak since there should be no CEF effect present, while for Tb^{3+} and Tm^{3+} atoms, on the other hand, it should be strong. Further investigation addressing these questions are planned.

VIII. CONCLUSION

The presented study introduces a new type of AlB_2 derived structure in which the R_2PdSi_3 (R = heavy rare earth) compounds crystallize. The complimentary use of neutron and x-ray diffraction in combination with EXAFS, DFT, and group theory excludes other structure solutions and determines the structure formation as a result of the ordering of Pd-Si atoms. It has been shown that the particularities of the structure can be understood in terms of energy minimization. The large Pd ion cannot have another Pd ion as nearest neighbor in the structure. Also, the Si ions are bound to form Hueckel arenes. These two rules lead to the stacking sequence of the four layers which form the R_2PdSi_3 structure.

The new unit cell contains 96 atoms compared to the three atoms of the primitive unit cell. Important for the magnetic properties are the two different rare earth sites in the structure. Especially the generic magnetic phase, which is unique for the R_2PdSi_3, can now be understood as the ordering of two sublattices within one crystallographic unit cell. The new structure might also lead to the re-interpretation of observed properties in other R_2TSi_3 compounds.

ACKNOWLEDGMENTS

The authors would like to thank H. Bitterlich, I. Mazilu, and G. Behr (Leibniz-Institut für Festkörper- und Werkstoffforschung Dresden) for crystal growth, G. Auffermann (Max-Planck-Institute for Chemical Physics of Solids, Dresden) for the ICP-OES investigation, Torsten Weissbach (Institut für Strukturphysik, TUD), Ch. Graf (Professur für Anorganische Chemie II, Technische Universität Dresden), and Barry Winn (Neutron Scattering Science Division, Oak Ridge National Laboratory) for valuable discussions. We gratefully acknowledge the financial support of DFG by the Sonderforschungsbereich 463 "Rare Earth-Transition-Metal-intermetallic compounds: Structure, Magnetism, Transport", the projects GE 1202/4-1 and 5-2, and the International Max Planck Research School for "Dynamical Processes in Atoms, Molecules and Solids." M.F. acknowledges the sponsorship of this research at Oak Ridge National Laboratory's Spallation Neutron Source by the Scientific User Facilities Division, Office of Basic Energy Sciences, U. S. Department of Energy. The kind hospitality granted by the Hahn-Meitner Institute in Berlin to perform neutron experiments is gratefully acknowledged.

APPENDIX A: THE FOURIER COMPONENTS OF THE SUPERSTRUCTURE

As inferred from the modulation vectors, the periodicity of the superstructure is $2 \times 2 \times 8$. Following Eq. (2), explicitly writing out the neutron scattering length $b_p(\boldsymbol{X})$ on the pth position in unit cell $\boldsymbol{X} = (0,0,z)$, $(1,0,z)$, $(1,1,z)$, and $(0,1,z)$ (since the analysis does not depend on the $\boldsymbol{r}_1$ or $\boldsymbol{r}_2$ positions in the unit cell, the subscript p will be omitted in the notation) yields

$$\begin{aligned}\delta b[\boldsymbol{X} = (0,0,z)] &= \sum_q \left(b_{\boldsymbol{\tau}_1^q} + b_{\boldsymbol{\tau}_2^q} + b_{\boldsymbol{\tau}_3^q}\right) e^{i2\pi\cdot z\cdot\frac{q}{8}} + \text{c.c.}, \\ \delta b[\boldsymbol{X} = (1,0,z)] &= \sum_q \left(-b_{\boldsymbol{\tau}_1^q} + b_{\boldsymbol{\tau}_2^q} - b_{\boldsymbol{\tau}_3^q}\right) e^{i2\pi\cdot z\cdot\frac{q}{8}} + \text{c.c.}, \\ \delta b[\boldsymbol{X} = (1,1,z)] &= \sum_q \left(-b_{\boldsymbol{\tau}_1^q} - b_{\boldsymbol{\tau}_2^q} + b_{\boldsymbol{\tau}_3^q}\right) e^{i2\pi\cdot z\cdot\frac{q}{8}} + \text{c.c.}, \\ \delta b[\boldsymbol{X} = (0,1,z)] &= \sum_q \left(b_{\boldsymbol{\tau}_1^q} - b_{\boldsymbol{\tau}_2^q} - b_{\boldsymbol{\tau}_3^q}\right) e^{i2\pi\cdot z\cdot\frac{q}{8}} + \text{c.c.} \end{aligned} \quad (A1)$$

The sequences on the four positions should be either sequence 1 or sequence 2, which can be expressed in Fourier expansion as in Eq. (A2), the respective Fourier components are listed in Table VIII,

$$b(z) = \frac{3b_{\text{Si}} + b_{\text{Pd}}}{4} + \frac{b_{\text{Si}} - b_{\text{Pd}}}{4} \sum_{k=1,2,3} c_k e^{i\phi_k} e^{i2\pi\cdot z\cdot\frac{k}{8}}. \quad (A2)$$

TABLE VIII. Fourier components and phase angles for the two sequences of six Si and two Pd atoms, for which the zeroth and fourth order components are zero.

	Sequence 1		
c_1^1	1.847759	ϕ_1^1	−2.74889
c_2^1	1.414214	ϕ_2^1	−2.35619
c_3^1	0.765367	ϕ_3^1	−1.96349
	Sequence 2		
c_1^2	0.765367	ϕ_1^2	−1.96349
c_2^2	1.414214	ϕ_2^2	2.35619
c_3^2	1.847759	ϕ_3^2	−2.74889

Comparing Eq. (A1) and (A2), the following equations can be written down:

$$\begin{aligned} b_{\boldsymbol{\tau}_1^q} + b_{\boldsymbol{\tau}_2^q} + b_{\boldsymbol{\tau}_3^q} &= b_q^1 e^{i\theta_q^1} e^{iq\psi_1}, \\ -b_{\boldsymbol{\tau}_1^q} + b_{\boldsymbol{\tau}_2^q} - b_{\boldsymbol{\tau}_3^q} &= b_q^2 e^{i\theta_q^2} e^{iq\psi_2}, \\ -b_{\boldsymbol{\tau}_1^q} - b_{\boldsymbol{\tau}_2^q} + b_{\boldsymbol{\tau}_3^q} &= b_q^3 e^{i\theta_q^3} e^{iq\psi_3}, \\ b_{\boldsymbol{\tau}_1^q} - b_{\boldsymbol{\tau}_2^q} - b_{\boldsymbol{\tau}_3^q} &= b_q^4 e^{i\theta_q^4} e^{iq\psi_4}, \end{aligned} \tag{A3}$$

where $q = 1, 2, 3$, $b_q^{j=1,2,3,4}$, and θ_q^j should take the values of one of the two sequences listed in Table VIII, ψ_j is the phase shift of the actual sequence on position $\boldsymbol{X}_j$ from the sequence 1 or 2 which can only take the value $n \cdot \frac{2\pi}{8}$ with n being integer.

Equation (A3) can be simplified to

$$\sum_{j=1}^{4} b_q^j e^{i\theta_q^j} e^{iq\psi_j} = 0, \tag{A4}$$

where j sums over the four positions in the doubled unit cell in the basal plane. Four kinds of solutions exist for the above equation as detailed below.

1. Type I solution

All b_q^j and θ_q^j take the values for sequence 1, for example, $b_q^j = c_q^1$ and $\theta_q^j = \phi_q^1$. Then Eq. (A4) can be further simplified to

$$\sum_{j=1}^{4} e^{iq\psi_j} = 0. \tag{A5}$$

There is an infinite choice of ψ_j which satisfy the above equation since, if $\{\psi_j\}$ is one set of a solution of the equation, then $\{\psi_j + \text{randomangle}\}$ would also be a solution. But they are physically equivalent. Therefore only the inequivalent solutions are presented here (same below). One solution of $\{\psi_j\}$ is $\psi_1 = 0$, $\psi_2 = \frac{\pi}{2}$, $\psi_3 = \pi$, $\psi_4 = \frac{3\pi}{2}$. The values for $b_{\boldsymbol{\tau}_i^k}$ are determined accordingly as listed in Table IX. Similarly, five other solutions can be found by permutation of $\{0, \frac{\pi}{2}, \pi, \frac{3\pi}{2}\}$ for ψ_j corresponding to the twinned domains due to $P6/mmm$ symmetry.

TABLE IX. Solution S1-1 of Fourier components for modulation vectors $b_{\boldsymbol{\tau}}$ when $\psi_1 = 0$, $\psi_2 = \frac{\pi}{2}$, $\psi_3 = \pi$, and $\psi_4 = \frac{3\pi}{2}$.

q	1	2	3
$b_{\boldsymbol{\tau}_1^q}$	$\frac{\sqrt{2}}{2} c_1^1 e^{i\phi_1^1} e^{-i\frac{\pi}{4}}$	0	$\frac{\sqrt{2}}{2} c_3^1 e^{i\phi_3^1} e^{i\frac{\pi}{4}}$
$b_{\boldsymbol{\tau}_2^q}$	$\frac{\sqrt{2}}{2} c_1^1 e^{i\phi_1^1} e^{i\frac{\pi}{4}}$	0	$\frac{\sqrt{2}}{2} c_3^1 e^{i\phi_3^1} e^{-i\frac{\pi}{4}}$
$b_{\boldsymbol{\tau}_3^q}$	0	$c_2^1 e^{i\phi_2^1}$	0

TABLE X. Type II solution of Fourier components for modulation vectors $b_{\boldsymbol{\tau}}$.

q	1	2	3
$b_{\boldsymbol{\tau}_1^q}$	$\frac{\sqrt{2}}{2} c_1^2 e^{i\phi_1^2} e^{-i\frac{\pi}{4}}$	0	$\frac{\sqrt{2}}{2} c_3^2 e^{i\phi_3^2} e^{i\frac{\pi}{4}}$
$b_{\boldsymbol{\tau}_2^q}$	$\frac{\sqrt{2}}{2} c_1^2 e^{i\phi_1^2} e^{i\frac{\pi}{4}}$	0	$\frac{\sqrt{2}}{2} c_3^2 e^{i\phi_3^2} e^{-i\frac{\pi}{4}}$
$b_{\boldsymbol{\tau}_3^q}$	0	$c_2^2 e^{i\phi_2^1}$	0

2. Type II solution

All b_q^j and θ_q^j take the values for sequence 2, that is, $b_q^j = c_k^2$ and $\theta_q^j = \phi_q^2$. Following similar analysis detailed above for solution 1, there are six symmetric equivalent solutions for $b_{\boldsymbol{\tau}_i^q}$, one of which is listed in Table X.

3. Type III solution

Each of the four $b_q^j e^{i\theta_q^j} e^{iq\psi^j}$ terms takes values in $\{c_q^2 e^{iq\phi_q^2}, c_q^2 e^{iq\phi_q^2} e^{iq\frac{\pi}{2}}, c_q^2 e^{iq\phi_q^2} e^{iq\frac{\pi}{4}}, c_q^1 e^{iq\phi_q^1} e^{iq\frac{3\pi}{2}}\}$. The permutation of $b_q^j e^{i\theta_q^j} e^{iq\psi^j}$ in the four possible values gives rise to 24 possible solutions. They can again be transformed into each other with the symmetry operations in the $P6/mmm$ group and are therefore considered to be symmetrically equivalent. One example for $b_{\boldsymbol{\tau}_i^q}$ is listed in Table XI.

4. Type IV solution

Each of the four $b_q^j e^{i\theta_q^j} e^{iq\psi^j}$ terms takes values in $\{c_q^1 e^{iq\phi_q^1}, c_q^1 e^{iq\phi_q^1} e^{iq\frac{\pi}{2}}, c_q^1 e^{iq\phi_q^1} e^{iq\frac{5\pi}{4}}, c_q^2 e^{iq\phi_q^2} e^{iq\pi}\}$. Similar to type III solution, there are 24 symmetry equivalent solutions of $b_{\boldsymbol{\tau}_s^q}$ as well. One of them is listed in Table XII.

APPENDIX B: SYMMETRY ANALYSIS

As discussed in the main text, there are only two possibilities for $b_{\boldsymbol{\tau},1}$ and $b_{\boldsymbol{\tau},2}$: $b_{\boldsymbol{\tau},1} = b_{\boldsymbol{\tau},2}$ with phase shift $\phi = 0$ as in representation Γ^1, or $b_{\boldsymbol{\tau},1} = -b_{\boldsymbol{\tau},2}$ with $\phi = \pi$ as in representation Γ^3. To preserve the sequences on the two sites as sequence 1 or 2, the phase shift for $b_{\boldsymbol{\tau}_1^q}$ should be $q\phi$. Thus

TABLE XI. Type III solution of Fourier components for modulation vectors $b_{\boldsymbol{\tau}}$.

q	1	2	3
$b_{\boldsymbol{\tau}_1^q}$	$\frac{c_1^2 e^{i\phi_1^2}(1+e^{i\frac{\pi}{4}})}{2}$	$\frac{c_2^2 e^{i\phi_2^2}(1+e^{i\frac{\pi}{2}})}{2}$	$\frac{c_3^2 e^{i\phi_3^2}(1+e^{i\frac{3\pi}{4}})}{2}$
$b_{\boldsymbol{\tau}_2^q}$	$\frac{c_1^2 e^{i\phi_1^2}(1+e^{i\frac{\pi}{2}})}{2}$	0	$\frac{c_3^2 e^{i\phi_3^2}(1+e^{i\frac{3\pi}{2}})}{2}$
$b_{\boldsymbol{\tau}_3^q}$	$\frac{c_1^2 e^{i\phi_1^2} + c_1^1 e^{i\phi_1^1} e^{i\frac{3\pi}{2}}}{2}$	$\frac{c_2^2 e^{i\phi_2^2} - c_2^1 e^{i\phi_2^1}}{2}$	$\frac{c_3^2 e^{i\phi_3^2} + c_3^1 e^{i\phi_3^1} e^{i\frac{\pi}{2}}}{2}$

TABLE XII. Type IV solution of Fourier components for modulation vectors $b_{\boldsymbol{\tau}}$.

q	1	2	3
$b_{\boldsymbol{\tau}_1^q}$	$\frac{c_1^1 e^{i\phi_1^1}(1+e^{i\frac{5\pi}{4}})}{2}$	$\frac{c_2^1 e^{i\phi_2^1}(1+e^{i\frac{\pi}{2}})}{2}$	$\frac{c_3^1 e^{i\phi_3^1}(1+e^{i\frac{-\pi}{4}})}{2}$
$b_{\boldsymbol{\tau}_2^q}$	$\frac{c_1^1 e^{i\phi_1^1}(1+e^{i\frac{\pi}{2}})}{2}$	0	$\frac{c_3^1 e^{i\phi_3^1}(1+e^{i\frac{3\pi}{2}})}{2}$
$b_{\boldsymbol{\tau}_3^q}$	$\frac{c_1^1 e^{i\phi_1^1}-c_1^2 e^{i\phi_1^2}}{2}$	$\frac{c_2^1 e^{i\phi_2^1}+c_2^1 e^{i\phi_2^1}}{2}$	$\frac{c_3^1 e^{i\phi_3^1}-c_3^2 e^{i\phi_3^2}}{2}$

we only need to consider the two possibilities for the relation between $b_{\boldsymbol{\tau}_s^1,1}$ and $b_{\boldsymbol{\tau}_s^1,2}$.

1. Case 1: $b_{\boldsymbol{\tau}_s^1}$ follows Γ^1 symmetry

When $b_{\boldsymbol{\tau}_s^1}$ follows the symmetry defined by the irreducible representation Γ^1, that is, $\phi = 0$, the phase shifts for both $b_{\boldsymbol{\tau}_s^{2,3}}$ are also zero, meaning $b_{\boldsymbol{\tau}_s^q,1} = b_{\boldsymbol{\tau}_s^q,2}$. The intensity for the superstructure reflections can be explicitly determined as follows:

$$F(\boldsymbol{Q}=\boldsymbol{G}+\boldsymbol{\tau}) = \sum_{\boldsymbol{r}_p} b_{\boldsymbol{\tau},p} e^{i(\boldsymbol{G}+\boldsymbol{\tau})\cdot\boldsymbol{r}_p}$$
$$= b_{\boldsymbol{\tau}} \cdot e^{i\pi(l+\tau_z)} \cdot e^{i2\pi\frac{h+k}{3}} \cdot e^{i2\pi\frac{\tau_x+\tau_y}{3}} \left(e^{i2\pi\frac{k+\tau_y}{3}} + e^{i2\pi\frac{h+\tau_x}{3}}\right), \tag{B1}$$

where $\boldsymbol{G}=(h,k,l)$, $\boldsymbol{\tau}=(\tau_x,\tau_y,\tau_z)$, $\boldsymbol{r}_1=(\frac{1}{3},\frac{2}{3},\frac{1}{2})$, and $\boldsymbol{r}_2=(\frac{2}{3},\frac{1}{3},\frac{1}{2})$ have been incorporated in the equation. When $2\pi\frac{k+\tau_y}{3} = 2\pi\frac{h+\tau_x}{3} + (2m+1)\pi$, $F(\boldsymbol{Q})=0$ which means that the reflections are extinct due to symmetry and the extinction condition is $k = h+\tau_x-\tau_y+3m+\frac{3}{2}$. For modulation vectors $\boldsymbol{\tau}_3^q$, $\tau_x=\tau_y=0.5$, the condition will never be satisfied; however for modulation vectors $\boldsymbol{\tau}_{1,2}^q$ the extinction condition is fulfilled at certain reflections.

Note that the extinction conditions differ with the different twinning domains and can be generated with the same symmetry operation, respectively. However, this extinction condition will extinct reflections with nonzero Fourier components. Thus, at reciprocal lattice points where the extinction condition is fulfilled, two of the six superstructure satellites will not be present [for example at $\boldsymbol{G}=(0,1,0)$, $\boldsymbol{\tau}_2^q$ will be missing]. This applies to all four types of solutions. But the experimental results showed otherwise: all six superstructure reflections were found around all measured main reflections including $\boldsymbol{G}=(0,1,0)$. So this case can be excluded.

2. Case 2: $b_{\boldsymbol{\tau}_s^1}$ follows Γ^3 symmetry

When $b_{\boldsymbol{\tau}_s^1}$ follows the symmetry defined by the irreducible representation Γ^3, that is, $\phi=\pi$, the phase shifts for $b_{\boldsymbol{\tau}_s^2}$ and $b_{\boldsymbol{\tau}_s^3}$ should be 2π and 3π, respectively, meaning $b_{\boldsymbol{\tau}_s^{1,3},1} = -b_{\boldsymbol{\tau}_s^{1,3},2}$ and $b_{\boldsymbol{\tau}_s^2,1} = b_{\boldsymbol{\tau}_s^2,2}$.

The extinction condition for Γ^1 symmetry has been derived previously in case 1: $k = h+\tau_x-\tau_y+3m+\frac{3}{2}$. For modulation vectors $b_{\boldsymbol{\tau}_{1,2}^2}$ this condition can be satisfied.

TABLE XIII. The averaged $|V(\boldsymbol{Q}=\boldsymbol{G}+\boldsymbol{\tau})|^2$ for each type of solutions. $\overline{|V(\boldsymbol{Q})|^2}$ of solution 1 and 2 do not depend on whether $k=h+3m$, $k=h+3m+1$ or $k=h+3m+2$, while for solutions 3 and 4 they matter because of the extinction conditions. The average has been performed over all the symmetric equivalent solutions in each type.

$(h,k,l)+\boldsymbol{\tau}$	τ_z	I	II	III	IV
$k=h+3m$	$\frac{1}{8}$	$\frac{1}{3}c_1^{1\,2}$	$\frac{1}{3}c_1^{2\,2}$	$\frac{1}{12}(4+\sqrt{2})c_1^{2\,2}$	$\frac{1}{12}(4-\sqrt{2})c_1^{1\,2}$
	$\frac{2}{8}$	$\frac{1}{3}c_2^{1\,2}$	$\frac{1}{3}c_2^{2\,2}$	$\frac{1}{3}c_2^{2\,2}$	$\frac{1}{3}c_2^{1\,2}$
	$\frac{3}{8}$	$\frac{1}{3}c_3^{1\,2}$	$\frac{1}{3}c_3^{2\,2}$	$\frac{1}{12}(4-\sqrt{2})c_3^{2\,2}$	$\frac{1}{12}(4+\sqrt{2})c_3^{1\,2}$
$k=h+3m+1$	$\frac{1}{8}$	$\frac{1}{3}c_1^{1\,2}$	$\frac{1}{3}c_1^{2\,2}$	$\frac{1}{6}(3+\sqrt{2})c_1^{2\,2}$	$\frac{1}{6}(3-\sqrt{2})c_1^{1\,2}$
	$\frac{2}{8}$	$\frac{1}{3}c_2^{1\,2}$	$\frac{1}{3}c_2^{2\,2}$	$\frac{1}{3}c_2^{2\,2}$	$\frac{1}{3}c_2^{1\,2}$
	$\frac{3}{8}$	$\frac{1}{3}c_3^{1\,2}$	$\frac{1}{3}c_3^{2\,2}$	$\frac{1}{6}(3-\sqrt{2})c_3^{2\,2}$	$\frac{1}{6}(3+\sqrt{2})c_3^{1\,2}$
$k=h+3m+2$	$\frac{1}{8}$	$\frac{1}{3}c_1^{1\,2}$	$\frac{1}{3}c_1^{2\,2}$	$\frac{1}{6}(3+\sqrt{2})c_1^{2\,2}$	$\frac{1}{6}(3-\sqrt{2})c_1^{1\,2}$
	$\frac{2}{8}$	$\frac{1}{3}c_2^{1\,2}$	$\frac{1}{3}c_2^{2\,2}$	$\frac{1}{6}c_2^{2\,2}$	$\frac{1}{6}c_2^{1\,2}$
	$\frac{3}{8}$	$\frac{1}{3}c_3^{1\,2}$	$\frac{1}{3}c_3^{2\,2}$	$\frac{1}{6}(3-\sqrt{2})c_3^{2\,2}$	$\frac{1}{6}(3+\sqrt{2})c_3^{1\,2}$

Similarly the intensity for the superstructure reflections can be deduced for Γ^3 symmetry as follows:

$$F(\boldsymbol{Q}=\boldsymbol{G}+\boldsymbol{\tau}) = \sum_{\boldsymbol{r}_p} b_{\boldsymbol{\tau},p} e^{i(\boldsymbol{G}+\boldsymbol{\tau})\cdot\boldsymbol{r}_p}$$
$$= b_{\boldsymbol{\tau}} \cdot e^{i\pi(l+\tau_z)} \cdot e^{i2\pi\frac{h+k}{3}} \cdot e^{i2\pi\frac{\tau_x+\tau_y}{3}} \left(e^{i2\pi\frac{k+\tau_y}{3}} - e^{i2\pi\frac{h+\tau_x}{3}}\right). \tag{B2}$$

The extinction condition now is $\frac{k+\tau_y}{3} = \frac{h+\tau_x}{3} + m \Rightarrow k = h+3m+\tau_x-\tau_y$. For modulation vectors $\boldsymbol{\tau}_{1,2}^q$, one of τ_x and τ_y is zero, so the condition will never be met. While for $\boldsymbol{\tau}_3^q$, $\tau_x=\tau_y=0.5$ the condition is met when $k=h+3m$. This applies to the $\frac{1}{8}$ and $\frac{3}{8}$ modulation vectors.

Type I and II solutions fit with the extinction conditions perfectly, where reflections are extinct by symmetry while their Fourier components are already zero. As a result from the averaging over the domains, no superstructure reflection will be missing. For type III and IV solutions the situation is more complicated and the intensities will depend on whether the extinction conditions are fulfilled.

In Table XIII the averaged $|F(\boldsymbol{Q}=\boldsymbol{G}+\boldsymbol{\tau})|^2$ are listed for the four solutions.

As can be seen from Table XIII, type I and IV solutions can be excluded because the intensities at $l=\frac{3}{8}n$ reflections are smaller than the intensities at $\frac{1}{8}$ which contradicts the experimental observation. Both type II and III solutions give smaller intensities for $\frac{1}{8}$ reflections, however, the ratio between $\frac{1}{8}$, $\frac{2}{8}$, and $\frac{3}{8}$ of type II solution is around 1:3.4:5.8 which is closer to experimental observations than solution 3 (1:2.5:2.8 for $k=h+3m$). Moreover, in solution 3 the superstructure reflections' intensities are different around $\boldsymbol{G}=(0,1,0)$ where $k=h+1$ and $\boldsymbol{G}=(0,-1,0)$ where $k=h+3\cdot(-1)+2$. This seems not to be the case. Also in type III solution, there exist two identical layers adjacent to each other, as shown by DFT calculations in the main text, this is energetically unstable. Thus we conclude that type II solution with $b_{\boldsymbol{\tau}_s^1}$ following Γ^3 symmetry is the correct solution.

*ftang@ifp.phy.tu-dresden.de

[1] T. Hahn (Ed.), *International Tables for Crystallography* (International Union of Crystallography, Chester, 2006), Chap. 7.1, Space group 191, p. 594.

[2] R.-D. Hoffmann and R. Pöttgen, Z. Kristallogr. **216**, 127 (2001).

[3] W. H. Zachariasen, Acta Crystallogr. **2**, 94 (1949).

[4] I. Mayer, E. Yanir, and I. Shidlovsky, Inorg. Chem. **6**, 842 (1967) [http://pubs.acs.org/doi/pdf/10.1021/ic50050a043].

[5] E. Houssay, A. Rouault, O. Thomas, R. Madar, and J. P. Senateur, Appl. Surf. Sci. **38**, 156 (1989).

[6] A. Iandelli, A. Palenzona, and G. L. Olcese, J. Less-Common Met. **64**, 213 (1979).

[7] R. Pöttgen and D. Kaczorowski, J. Alloys Compd. **201**, 157 (1993).

[8] B. Chevalier, R. Pöttgen, B. Darriet, P. Gravereau, and J. Etourneau, J. Alloys Compd. **233**, 150 (1996).

[9] R. Pöttgen, P. Gravereau, B. Darriet, B. Chevalier, E. Hickey, and J. Etourneau, J. Mater. Chem. **4**, 463 (1994).

[10] K. Yubuta, T. Yamamura, and Y. Shiokawa, J. Phys. Condens. Matter **18**, 6109 (2006).

[11] R. Gordon, C. Warren, M. Alexander, F. DiSalvo, and R. Pöttgen, J. Alloys Compd. **248**, 24 (1997).

[12] B. Chevalier, P. Lejay, J. Etourneau, and P. Hagenmuller, Solid State Commun. **49**, 753 (1984).

[13] N. Sato, M. Kagawa, K. Tanaka, N. Takeda, T. Satoh, S. Sakatsume, and T. Komatsubara, J. Phys. Soc. Jpn. **60**, 757 (1991).

[14] S. Majumdar, E. Sampathkumaran, M. Brando, J. Hemberger, and A. Loidl, J. Magn. Magn. Mater. **236**, 99 (2001).

[15] K. Yubuta, T. Yamamura, D. Li, and Y. Shiokawa, Solid State Commun. **149**, 286 (2009).

[16] M. deL. Pinto, Acta Crystallogr. **21**, 999 (1966).

[17] A. Kimura, D. Li, and Y. Shiokawa, Solid State Commun. **113**, 131 (1999).

[18] J. C. Slater, J. Chem. Phys. **41**, 3199 (1964).

[19] P. A. Kotsanidis, J. K. Yakinthos, and E. Gamari-Seale, J. Magn. Magn. Mater. **87**, 199 (1990).

[20] A. Szytula, M. Hofmann, B. Penc, M. Slaski, S. Majumdar, E. V. Sampathkumaran, and A. Zygmunt, J. Magn. Magn. Mater. **202**, 365 (1999).

[21] R. Mallik and E. V. Sampathkumaran, J. Magn. Magn. Mater. **164**, L13 (1996).

[22] R. Mallik, E. V. Sampathkumaran, and P. L. Paulose, Solid State Commun. **106**, 169 (1998).

[23] R. Mallik, E. V. Sampathkumaran, M. Strecker, and G. Wortmann, Europhys. Lett. **41**, 315 (1998).

[24] S. Majumdar, E. V. Sampathkumaran, P. L. Paulose, H. Bitterlich, W. Löser, and G. Behr, Phys. Rev. B **62**, 14207 (2000).

[25] S. Majumdar, H. Bitterlich, G. Behr, W. Löser, P. L. Paulose, and E. V. Sampathkumaran, Phys. Rev. B **64**, 012418 (2001).

[26] E. V. Sampathkumaran, H. Bitterlich, K. K. Iyer, W. Löser, and G. Behr, Phys. Rev. B **66**, 052409 (2002).

[27] M. Frontzek, Ph.D. thesis, TU Dresden, 2009 [http://nbn-resolving.de/urn:nbn:de:bsz:14-qucosa-24779].

[28] P. G. D. Gennes, J. Phys. Radium **23** (1962).

[29] R. A. Gordon, C. J. Warren, M. Alexander, F. DiSalvo, and R. Pöttgen, J. Alloys Compd. **248**, 24 (1997).

[30] G. Graw, H. Bitterlich, W. Löser, G. Behr, J. Fink, and L. Schultz, J. Alloys Compd. **308**, 193 (2000).

[31] H. Bitterlich, Ph.D. thesis, TU Dresden, 2000.

[32] I. Mazilu, M. Frontzek, W. Löser, G. Behr, A. Teresiak, and L. Schultz, J. Cryst. Growth **275**, e103 (2005).

[33] M. Frontzek, A. Kreyssig, M. Doerr, J. U. Hoffman, D. Hohlwein, H. Bitterlich, G. Behr, and M. Loewenhaupt, Physica B **350**, e187 (2004).

[34] M. Frontzek, A. Kreyssig, M. Doerr, M. Rotter, G. Behr, W. Löser, I. Mazilu, and M. Loewenhaupt, J. Magn. Magn. Mater. **301**, 398 (2006).

[35] M. Frontzek, A. Kreyssig,, M. Doerr, A. Schneidewind, J.-U. Hoffmann, and M. Loewenhaupt, J. Phys. Condens. Matter **19**, 145276 (2007).

[36] D. S. Inosov, D. V. Evtushinsky, A. Koitzsch, V. B. Zabolotnyy, S. V. Borisenko, A. A. Kordyuk, M. Frontzek, M. Loewenhaupt, W. Löser, I. Mazilu, H. Bitterlich, G. Behr, J. U. Hoffmann, R. Follath, and B. Büchner, Phys. Rev. Lett. **102**, 046401 (2009).

[37] J. Dshemuchadse, Diplomarbeit, TU Dresden, 2008.

[38] M. Frontzek, F. Tang, P. Link, A. Schneidewind, J. M. Mignot, J. U. Hoffman, and M. Loewenhaupt, J. Phys.: Conf. Ser. **251**, 012026 (2010).

[39] Y. Xu, W. Löser, G. Behr, M. Frontzek, F. Tang, B. Büchner, and L. Liu, J. Cryst. Growth **312**, 1992 (2010).

[40] G. Behr and W. Löser, Recent Research and Development in Crystal Growth, Transworld Research Network, Trivandrum **4**, 129 (2005).

[41] T. Leisegang, Ph.D. thesis, TU Dresden, 2010.

[42] T. Weissbach, T. Leisegang, A. Kreyssig, M. Frontzek, J.-U. Hoffmann, D. Souptel, A. Köhler, G. Behr, P. Paufler, and D. C. Meyer, J. Appl. Crystallogr. **41**, 738 (2008).

[43] V. Petricek, M. Dusek, and L. Palatinus, JANA 2006—The Crystallographic Computing System (2006), http://jana.fzu.cz/.

[44] P. A. Lee, P. H. Citrin, P. Eisenberger, and B. M. Kincaid, Rev. Mod. Phys. **53**, 769 (1981).

[45] K. Rickers, U. Brüggmann, W. Drube, M. Herrmann, J. Heuer, E. Welter, H. Schulte-Schrepping, and H. Schulz-Ritter, AIP Conf. Proc. **879**, 907 (2007).

[46] K. Rickers, W. Drube, H. Schulte-Schrepping, E. Welter, U. Brüggmann, M. Herrmann, J. Heuer, and H. Schulz-Ritter, AIP Conf. Proc. **882**, 905 (2007).

[47] K. V. Klementiev, XAFSMASS, freeware [www.desy.de/klmn/xafsmass.html] (2003).

[48] B. Ravel and M. Newville, J. Synchrotron Radiat. **12**, 537 (2005).

[49] S. I. Zabinsky, J. J. Rehr, A. Ankudinov, R. C. Albers, and M. J. Eller, Phys. Rev. B **52**, 2995 (1995).

[50] G. Kresse and D. Joubert, Phys. Rev. B **59**, 1758 (1999).

[51] J. P. Perdew, J. A. Chevary, S. H. Vosko, K. A. Jackson, M. R. Pederson, D. J. Singh, and C. Fiolhais, Phys. Rev. B **46**, 6671 (1992).

[52] G. Kresse and J. Furthmüller, Comput. Mater. Sci. **6**, 15 (1996).

[53] A. G. McKale, B. W. Veal, A. P. Paulikas, S. K. Chan, and G. S. Knapp, J. Am. Chem. Soc. **110**, 3763 (1988) [http://pubs.acs.org/doi/pdf/10.1021/ja00220a008].

[54] V. M. Nield and D. A. Keen, *Diffuse Neutron Scattering from Crystalline Materials* (Oxford Science, Oxford, 2001).

[55] T. R. Welberry and B. D. Butler, J. Appl. Crystallogr. **27**, 205 (1994).

[56] J. M. Pérez-Mato, G. Madariaga, and M. J. Tello, J. Phys. C **19**, 2613 (1986).

[57] K. Dornberger-Schiff, Acta Crystallogr. **9**, 593 (1956).
[58] F. Tang, Ph.D. thesis, TU Dresden, 2010 [http://nbn-resolving.de/urn:nbn:de:bsz:14-qucosa-64225].
[59] F. Tang, P. Link, M. Frontzek, A. Schneidewind, W. Löser, and M. Loewenhaupt, J. Phys.: Conf. Ser. **251**, 012004 (2010).
[60] M. Frontzek, F. Tang, P. Link, A. Schneidewind, J.-U. Hoffman, J.-M. Mignot, and M. Loewenhaupt, Phys. Rev. B **82**, 174401 (2010).
[61] F. Tang, P. Link, M. Frontzek, J.-M. Mignot, J.-U. Hoffmann, W. Löser, and M. Loewenhaupt, J. Phys.: Conf. Ser. **251**, 012017 (2010).